Tribology International 209 (2025) 110731

Contents lists available at ScienceDirect

Tribology International

journal homepage: www.elsevier.com/locate/triboint

Full Length Article

Continuum modeling of dislocation microstructures under tribological loading

Sing-Huei Lee [a,b], Christian Wieners [c], Katrin Schulz [a,b,*]

[a] Karlsruhe Institute of Technology (KIT), Institute for Applied Materials (IAM), Karlsruhe, Germany
[b] Karlsruhe University of Applied Sciences (HKA), Karlsruhe, Germany
[c] Karlsruhe Institute of Technology (KIT), Institute for Applied and Numerical Mathematics (IANM), Karlsruhe, Germany

ARTICLE INFO

Dataset link: https://gitlab.kit.edu/kit/mpp

Keywords:
Dislocation-based crystal plasticity
Continuum dislocation dynamics
Tribological loading
Dislocation trace line

ABSTRACT

Dislocation-mediated plastic deformation governs the mechanical response and microstructural evolution in tribological contacts, yet linking these effects across scales remains challenging. We present a dislocation-based crystal plasticity model that couples micro-scale dislocation dynamics with macro-scale plastic deformation under sliding conditions. By incorporating crystallographic effects on dislocation mobility and capturing subsurface dislocation transport and trace line formation, the model reveals intricate microstructural features that influence plastic deformation, surface topography, and contact area evolution. Unlike continuum-scale simulations, which lack the resolution to capture microstructural details, or discrete simulations, which fail to couple microstructure-driven plasticity with tribological contact, this model bridges these gaps. Leveraging an implicit macro–micro coupling mechanism, a flux vector splitting-based numerical scheme, and a penalty contact boundary condition, this work provides a foundation for predictive modeling capturing dislocation-driven deformation under tribological contact.

1. Introduction

Plastic deformation is a key factor influencing tribological contact mechanics [1–4], as it determines surface topography and stress distribution during sliding. To accurately predict plastic deformation in tribological contact scenarios, dislocation characteristics must be carefully considered, as dislocation glide is a primary mechanism driving plastic deformation.

Main dislocation processes induced by tribological loading include dislocation transport phenomena, where dislocations are retained within the stress field beneath the moving asperity and move along with the sliding motions, as demonstrated by [2] using discrete dislocation dynamic (DDD) simulations. Additionally, the formation of one or more dislocation trace lines (DTLs) parallel to the sliding direction, representing accumulated dislocation densities at specific depths, indicates discrete crystal rotation changes. And the discontinuities in crystal orientations further result in the formation of sub-grains. This phenomenon has been widely observed in experimental studies [5–7].

A similar loading scenario is the indentation loading. At the scale of single crystalline materials, existing modeling approaches include continuum crystal plasticity models [8–11], DDD [2–4,12], and molecular dynamics (MD) [13–17]. The main challenge in predicting material response under tribological contact using continuum crystal plasticity methods lies in their assumption that plastic strain occurs only when the applied stress exceeds a threshold. These methods neglect the detailed motion and dynamics of dislocations. [2] points out that the continuum approaches fail to effectively account for dislocation transport. Likewise, [3] notes that a surface pile-up, the result of plastic deformation under tribology loading, strongly depends on the crystal orientation. However, standard crystal plasticity methods are less sensitive to crystallographic effects and tend to underestimate pile-ups compared to discrete simulations. This limitation arises from the coarse-graining process, which reduces the localization of plastic mechanisms compared to discrete level simulations. However, another challenge arises in discrete-level simulations, which often simplify tribological contact using superposed analytical solutions, such as the Green's function method [18]. These models typically assume purely elastic deformation and idealized geometries. For instance, Hamilton's solution [19] predicts stress fields for a spherical surface sliding against a semi-infinite plane, resulting in a circular contact area. However, such models neglect plastic deformation and changes in surface geometry during sliding, leading to inaccuracies in stress field predictions once plastic deformation occurs. Additionally, as highlighted in [4], elastic models often estimate that under small loads, the true contact area

* Corresponding author at: Karlsruhe Institute of Technology (KIT), Institute for Applied Materials (IAM), Karlsruhe, Germany.
E-mail address: katrin.schulz@kit.edu (K. Schulz).

https://doi.org/10.1016/j.triboint.2025.110731
Received 17 January 2025; Received in revised form 14 April 2025; Accepted 15 April 2025
Available online 25 April 2025
0301-679X/© 2025 The Authors. Published by Elsevier Ltd. This is an open access article under the CC BY-NC-ND license (http://creativecommons.org/licenses/by-nc-nd/4.0/).

Nomenclature

$\boldsymbol{\beta}_{\mathrm{el}}$, $\boldsymbol{\beta}_{\mathrm{pl}}$	Elastic and plastic part of displacement gradient
$\boldsymbol{\kappa}^{\mathrm{s}}$, $\kappa^{\mathrm{s}}_{\mathrm{screw}}$, $\kappa^{\mathrm{s}}_{\mathrm{edge}}$	Vector of the GND density and its screw and edge component on slip system s
$\boldsymbol{\kappa}^{\mathrm{s}}_{\perp}$	Orthogonal vector of the GND density of slip system s
$\boldsymbol{\sigma}$	Cauchy stress tensor
$\boldsymbol{\varepsilon}_{\mathrm{tot}}$, $\boldsymbol{\varepsilon}_{\mathrm{el}}$, $\boldsymbol{\varepsilon}_{\mathrm{pl}}$	Total, elastic and plastic strain
$\boldsymbol{f}_{\mathcal{B}}$	Body force
$\boldsymbol{n}_{\partial\mathcal{B}}$	The surface normal of the domain $\partial\mathcal{B}$
$\boldsymbol{t}_{\mathrm{S}}$	Prescribed surface traction (Neumann boundary condition)
$\boldsymbol{t}_{\mathrm{N}}$, $\boldsymbol{t}_{\mathrm{F}}$	Normal and tangential surface traction
$\boldsymbol{u}$	Displacement field
$\boldsymbol{u}_{\mathrm{D}}$	Prescribed displacement (Dirichlet boundary condition)
ℓ_{elem}	Element size
γ^{s}	Plastic slip of slip system s
Γ_c	The domain for the contact surface
$\lambda^{(\ell)\alpha}_{\phi}$, $\mathbf{K}^{(\ell)}_{\phi}$	The ℓth eigenvalue and its corresponding eigenvector with the sign α along the direction ϕ
$\left(\mathbf{F}^{*\alpha}_{i}\right)_{\phi}$	Numerical flux with the sign α in element i along the direction ϕ
$\mathbb{C}$	Anisotropic elasticity tensor
$\mathbf{A}^{\mathrm{s}}$	Dislocation alignment tensor of slip system s
$\mathbf{C}_{\mathrm{indent}}$, $\mathrm{R}_{\mathrm{indent}}$	The center coordinate and radius of the indenter
$\mathbf{J}_{\phi}$	The Jacobian matrix split along the direction ϕ
$\mathbf{M}^{\mathrm{s}}$	Schmidt tensor
$\mathbf{N}_{\mathrm{f}}$	The face outward normal for face of element located at (i, j, k) for face f
$\mathbf{Q}_i$	The unknown vector for CDD PDEs $\left(\left[\rho^{\mathrm{s}}, \boldsymbol{\kappa}^{\mathrm{s}}\cdot\mathbf{l}^{\mathrm{s}}, \boldsymbol{\kappa}^{\mathrm{s}}\cdot\mathbf{d}^{\mathrm{s}}, \mathrm{q}^{\mathrm{s}}\right]^{T}\right)$ in element i
$\mathbf{x}_{\mathrm{projected}}$	The projected point on the indenter for node $\mathbf{x}$
$\mathcal{F}_{\mathrm{applied}}$	The applied force on the indenter
$\mathcal{G}(\mathbf{x})$	The gap function for node $\mathbf{x}$
$\mathcal{K}_{ij}$, α_{ij}	Lattice curvature and dislocation (Nye's) tensor
$\mathrm{L}_{\mathrm{stroke}}$	The stroke length of sliding
q^{s}	Dislocation curvature density of slip system s
$\mathrm{v}_{\mathrm{slid}}$	The sliding speed of indenter
μ, ν	Shear modulus and Poisson's ratio
μ_{friction}	Coulomb friction coefficient
ω_0	Penalty parameter
$\partial\mathcal{B}_{\mathrm{D}}$, $\partial\mathcal{B}_{\mathrm{N}}$	Domains applied Dirichlet and Neumann boundary condition
ρ^{s}	Mobile dislocation density on slip system s
$\rho^{\mathrm{s}}_{\mathrm{SSD}}$	Statistically stored dislocation density on slip system s
τ^{s}	The effective resolved shear stress of slip system s
$\tau^{\mathrm{s}}_{\mathrm{ext}}$, $\tau^{\mathrm{s}}_{\mathrm{int}}$	Resolved shear stress due to external loading and internal interaction on slip system s
$\tau^{\mathrm{s}}_{\mathrm{mf}}$, $\tau^{\mathrm{s}}_{\mathrm{b}}$	Mean field stress and back stress on slip system s
$\tau^{\mathrm{s}}_{\mathrm{y}}$	The yield stress of slip system s
$\mathbf{b}^{\mathrm{s}}$, b^{s}	Burger's vector and its length of slip system s
$\mathbf{d}_{\mathrm{indent}}$	Sliding direction of the indenter
B	Drag coefficient of the velocity law
L_x, L_y, L_z	x, y, and z dimension of the material
$\mathrm{M}_{\mathrm{indent}}$	The iteration scaling factor for contact search
v^{s}	Isotropic dislocation velocity on slip system s
φ_x, φ_y, φ_z	Crystal rotation around the x−(SD), y−(ND), and z−directions
ξ_{force}, ξ_{y}	Iteration tolerance for macro scale force balance and implicit coupling
ξ_{indent}	Iteration tolerance for the force balance on the indenter
$\{\mathbf{d}^{\mathrm{s}}, \mathbf{l}^{\mathrm{s}}, \mathbf{m}^{\mathrm{s}}\}$	The orthonormal basis of slip system s
a_{gs}	Interaction parameters for latent hardening between slip systems s and g
D'	Material parameter for $\tau^{\mathrm{s}}_{\mathrm{b}}$
T, $\triangle T$	Time and time step size for the macro time series
t, $\triangle t$	Time and time step size for the micro time series
N, M	Discretization number of macro and micro time series

is much smaller than the nominal contact area, with contact pressure significantly exceeding the nominal pressure.

In this study, we introduce a dislocation-based crystal plasticity model based on the continuum dislocation dynamics (CDD) approach, embedded into a numerical efficient simulation framework to analyze macro- and micro-scale material behavior considering tribological contact mechanics. To enhance numerical stability, we derived a numerical scheme using the flux vector splitting method for solving CDD problems. An implicit coupling mechanism was implemented, enabling larger simulation time steps and accurately capturing the influence of dislocation evolution on plastic deformation. To model material responses under tribological contact conditions, we introduced a penalty contact method with a Neumann boundary condition. We show that this approach effectively bridges the gap between macro- and micro-scale behaviors in tribological contact mechanics. Our model successfully simulates the accumulation of geometrically necessary dislocation (GND) densities beneath the indented surface, aligning with the locations of DTLs observed in experiments. It also captures dislocation transport phenomena and the plastic deformation induced by microstructural evolution under both symmetrical and asymmetrical crystal orientations.

2. Methodology

In this section, we introduce the dislocation-based crystal plasticity formulation using CDD theory. We outline the numerical scheme with a focus on deriving numerical fluxes for the partial differential equations in a CDD problem and the implicit coupling between macro- and micro-scales. Additionally, we detail the boundary conditions applied to model tribological contact, also the material parameters and system setup used in this study. The plasticity model is implemented using

the M++ library [20], a parallel finite element software optimized for high-performance computing environments.

2.1. Fundamental of continuum dislocation dynamic based crystal plasticity model

We decompose the deformation gradient tensor ($D\boldsymbol{u}$) into an elastic ($\boldsymbol{\beta}_{el}$) and a plastic ($\boldsymbol{\beta}_{pl}$) component as

$$D\boldsymbol{u} = \boldsymbol{\beta}_{el} + \boldsymbol{\beta}_{pl}. \tag{1}$$

Here, $\boldsymbol{u}$ denotes the displacement field. The total infinitesimal strain $\boldsymbol{\varepsilon}_{tot}$ is defined as $\boldsymbol{\varepsilon}_{tot} = \mathrm{sym}(D\boldsymbol{u})$, where the elastic strain $\boldsymbol{\varepsilon}_{el}$ is $\boldsymbol{\varepsilon}_{el} = \mathrm{sym}(\boldsymbol{\beta}_{el})$, and the plastic strain $\boldsymbol{\varepsilon}_{pl}$ is $\boldsymbol{\varepsilon}_{pl} = \mathrm{sym}(\boldsymbol{\beta}_{pl})$. The macro force equilibrium equation with the body force $\boldsymbol{f}_{\mathcal{B}}$ is expressed as

$$-\nabla \cdot \boldsymbol{\sigma} = \boldsymbol{f}_{\mathcal{B}}, \tag{2}$$

where $\boldsymbol{\sigma}$ represents the Cauchy stress tensor, given by $\boldsymbol{\sigma} = \mathbb{C}\left[\boldsymbol{\varepsilon}_{tot} - \boldsymbol{\varepsilon}_{pl}\right]$, and $\mathbb{C}$ is the anisotropic elasticity tensor. The boundary conditions necessary for resolving Eq. (2) include the Dirichlet boundary condition (Eq. (3a)) for prescribed displacement field $\boldsymbol{u}_D$ on $\partial\mathcal{B}_D$ and Neumann boundary condition (Eq. (3b)) for prescribed surface traction $\boldsymbol{t}_S$ on $\partial\mathcal{B}_N$

$$\boldsymbol{u} = \boldsymbol{u}_D \quad \text{on } \partial\mathcal{B}_D \tag{3a}$$

$$\boldsymbol{\sigma} \cdot \boldsymbol{n}_{\partial\mathcal{B}} = \boldsymbol{t}_S \quad \text{on } \partial\mathcal{B}_N, \tag{3b}$$

where $\boldsymbol{n}_{\partial\mathcal{B}}$ is the surface normal of the domain $\partial\mathcal{B}$. The plastic strain $\boldsymbol{\varepsilon}_{pl}$ can be determined by calculating $\boldsymbol{\beta}_{pl}$ based on the microstructure evolution. The plastic distortion tensor $\boldsymbol{\beta}_{pl}$ is obtained by summing the plastic slip, γ^s of a slip system s, across all slip systems

$$\boldsymbol{\beta}_{pl} = \sum_{s=1}^{N} \gamma^s \mathbf{M}^s \tag{4}$$

where $\mathbf{M}^s$ is the Schmidt tensor, $\mathbf{M}^s = \mathbf{d}^s \otimes \mathbf{m}^s$. In this context, the orientations of the slip systems are defined by the orthonormal basis $\{\mathbf{d}^s, \mathbf{l}^s, \mathbf{m}^s\}$ based on the face-centered cubic (FCC) crystal structure, where $\mathbf{m}^s$ is the slip plane normal and $\mathbf{d}^s = \frac{1}{b^s}\mathbf{b}^s$ is the slip direction. Here, $\mathbf{b}^s$ is the Burger's vector with length b^s, and $\mathbf{l}^s = \mathbf{m}^s \times \mathbf{d}^s$ is the line direction. The plastic slip γ^s arises from dislocation motion on the slip system s, linking dislocation motion to plastic deformation. According to Orowan's equation, the plastic slip rate $\partial_t\gamma^s$ can be calculated by the following equation

$$\partial_t\gamma^s = v^s b^s \rho^s, \tag{5}$$

where v^s is the isotropic dislocation velocity, and ρ^s is the mobile dislocation density on slip system s. The mobile dislocation density ρ^s consists of the statistically stored dislocation (SSD) density ρ^s_{SSD} and the GND density

$$\rho^s = |\boldsymbol{\kappa}^s| + \rho^s_{SSD}, \tag{6}$$

where $\boldsymbol{\kappa}^s = \kappa^s_{screw}\mathbf{d}^s + \kappa^s_{edge}\mathbf{l}^s$ denotes the vector of the GND density. Based on the CDD formulation in [21], the evolution of ρ^s, $\boldsymbol{\kappa}^s$, and the dislocation curvature density q^s is governed by the following PDEs

$$\partial_t\rho^s = -\nabla \cdot (v^s \boldsymbol{\kappa}^s_\perp) + v^s q^s \quad \text{with} \quad \boldsymbol{\kappa}^s_\perp = \boldsymbol{\kappa}^s \times \boldsymbol{m}^s, \tag{7a}$$

$$\partial_t\boldsymbol{\kappa}^s = \nabla \times (\rho^s v^s \boldsymbol{m}^s), \tag{7b}$$

$$\partial_t q^s = -\nabla \cdot \left(\frac{q^s}{\rho^s}\boldsymbol{\kappa}^s_\perp v^s + \mathbf{A}^s \nabla v^s\right). \tag{7c}$$

Modeling the evolution of q^s, we employ the closure assumptions according to [22], with the dislocation alignment tensor $\mathbf{A}^s$ given by

$$\mathbf{A}^s = \frac{1}{2|\boldsymbol{\kappa}^s|^2}\left(\left(\rho^s + |\boldsymbol{\kappa}^s|\right)\boldsymbol{\kappa}^s \otimes \boldsymbol{\kappa}^s + \left(\rho^s - |\boldsymbol{\kappa}^s|\right)\boldsymbol{\kappa}^s_\perp \otimes \boldsymbol{\kappa}^s_\perp\right) \tag{8}$$

(following the notation in [23]). The dislocation curvature density, derived from high-dimensional CDD theory [21], represents the sum of the local curvatures of all dislocation lines contained within the volume.

To calculate v^s on slip system s in Eqs. (5) and (7), a formulation for the velocity law is needed to characterize the relationship between the stress state and v^s. Following [22], we assume a linear-viscous model of over-damped dislocation motion. Therefore, a linear dependency between the effective resolved shear stress τ^s and v^s is applied if τ^s exceeds the yield stress τ^s_y on the slip system. The velocity law can be expressed as

$$v^s = \begin{cases} \frac{b^s}{B}(|\tau^s| - \tau^s_y)\,\mathrm{sign}(\tau^s) & \text{if } |\tau^s| > \tau^s_y \\ 0 & \text{if } |\tau^s| \le \tau^s_y. \end{cases} \tag{9}$$

Here, B is the drag coefficient.

τ^s can be expressed as the superposition of shear stress due to external loading τ^s_{ext} and internal shear stresses τ^s_{int} of the microstructure

$$\tau^s = \tau^s_{ext} + \tau^s_{int}. \tag{10}$$

τ^s_{ext} is the projection of $\boldsymbol{\sigma}$ on slip system s via the Schmidt law, $\tau^s_{ext} = \boldsymbol{\sigma} : \mathbf{M}^s$. The internal stress $\tau^s_{int} = \tau^s_b + \tau^s_{mf}$ is divided into a long-range (mean field stress, τ^s_{mf}) and a short-range (back stress, τ^s_b) component. τ^s_{mf} is the stress induced by a mean-field approach to maintain geometric consistency across coarse-grained volumes, as described in [24]. For systems with strong gradients of plastic distortion, the model can be enhanced by introducing short-range correction stresses τ^s_b as proposed by [25,26] as the back stress term, and it is given by

$$\tau^s_b = \frac{\mu b^s}{2\pi(1-\nu)} D' \left(\frac{\nabla\kappa^s_{edge}}{\rho^s_{SSD}}\right) \tag{11}$$

with

$$D' = 0.0588\,\ell_{elem}\sqrt{\kappa^s_{edge}}\,tan^{-1}\left(\ell_{elem}\sqrt{\kappa^s_{edge}}\right), \tag{12}$$

where ℓ_{elem} is the size of an averaging volume, i.e. the size of an element. μ is the shear modulus and ν is the Poisson's ratio.

The yield stress τ^s_y incorporates Franciosi's formulation to include latent hardening, accounting for hardening effects due to interactions among different slip systems [27]. This formulation uses a matrix of interaction parameters a_{gs}, considering interactions in addition to Taylor-type hardening [28]. The expression for the individual yield stress τ^s_y on slip system s is given by

$$\tau^s_y = \sum_g \tau^y_{gs} = \sum_g a_{gs}\mu b^s \sqrt{\rho^s}, \tag{13}$$

where τ^y_{gs} represents the latent hardening from interactions between slip systems g and s. For FCC crystals, the matrix a_{gs} includes six coefficients, reflecting different types of reactions such as Lomer locks, Hirth locks, and glissile junctions for forest interactions, along with self, coplanar, and collinear interactions.

2.2. Discretization scheme of the macro and micro problem

The model is divided into a macro and a micro problem. The macro problem involves solving the force equilibrium (Eq. (2)), while the micro problem addresses the CDD problem (Eq. (7)). These two scales are interconnected through the micro-state variable γ^s and the macro-state variable v^s using Orowan's equation (Eq. (5)) on each slip system s.

In the following, we describe the discretization scheme for both the macro and micro problems (Eq. (2)) as well as the approximation of the system discretized using a typical semi-discrete approach. We consider the discretization process in two stages, first discretizing the PDEs only in space and then discretizing in time.

For the space discretization, the macro problem is discretized over the spatial domain using a conforming finite element method with Lagrange discretization [29] to retain the continuity of macroscopic field variables such as displacement, stress, strain, and dislocation velocity.

Then, the resulting semi-discrete system is discretized and solved using a nonlinear time integrator with the implicit Euler method [30].

The micro (CDD) problem, as shown in Eq. (7), consists of a set of hyperbolic partial differential equations (PDEs) describing dislocation evolutions. Unlike the macro problem, the PDEs for the micro problem are firstly discretized over the spatial domain using the discontinuous Galerkin method [31,32] to retain mass conservation while resolving dislocation dynamics. The resulting system is then solved using a diagonal implicit Runge–Kutta scheme time integrator [33].

For the time discretization, the time series for the macroscopic problem is denoted as T. This series consists of discrete time points T such that $T \in \{0, \dots, T_{\mathrm{n}}, \dots, T_{\mathrm{N}}\}$, where $T_{\mathrm{n}} = \mathrm{n} \cdot \triangle T$ and $\triangle T$ is the step size for the macro time series. For the microscopic problem, the time series is denoted as t. This series consists of discrete time points t such that $t \in \{0, \dots, t_{\mathrm{m}}, \dots, t_{\mathrm{M}}\}$ within the span of one macro time step, where $t_{\mathrm{m}} = \mathrm{m} \cdot \triangle t$ and $\triangle t$ is the step size for the micro time series. To distinguish the micro time steps within each macro time step, we use the notation $t^{\mathrm{n}}_{\mathrm{m}} = T_{\mathrm{n}} + \mathrm{m} \cdot \triangle t$. This relationship can be represented as

$$\left\{T_0,\, t^0_1,\, \dots,\, t^0_{\mathrm{m}},\, \dots,\, t^0_{\mathrm{M}} = T_1,\, \dots,\, t^1_m,\, \dots,\, t^1_M = T_2,\, \dots,\, T_{\mathrm{n}},\, \dots,\, T_{\mathrm{N}}\right\}. \quad (14)$$

For both macro and micro problem, within each time step, the problems are approximated linearly. Each linear system is solved iteratively using the generalized minimal residual (GMRES) method [34].

We now describe the approximation system for the micro (CDD) problem. Following the derivation of [22,35], the evolution of the dislocation field variables in a single slip system s can be evaluated by resolving the PDEs of a CDD problem (Eq. (7)) within one micro time step, the CDD problem for each slip system s can be written as

$$\partial_{\mathrm{t}}\mathbf{Q}(x,y,z,t) + \nabla\mathbf{F}\left(\mathbf{Q}(x,y,z,t)\right) = \mathbf{S}\left(\mathbf{Q}(x,y,z,t)\right), \quad (15)$$

where the unknown vector is $\mathbf{Q} = \left[\rho^{\mathrm{s}}, \boldsymbol{\kappa}^{\mathrm{s}} \cdot \mathbf{l}^{\mathrm{s}}, \boldsymbol{\kappa}^{\mathrm{s}} \cdot \mathbf{d}^{\mathrm{s}}, \mathrm{q}^{\mathrm{s}}\right]^T$. The flux vector $\mathbf{F}(\mathbf{Q})$ and the source vector $\mathbf{S}(\mathbf{Q})$ are both given as

$$\mathbf{F}(\mathbf{Q}) = \begin{bmatrix} \mathrm{v}^{\mathrm{s}}\boldsymbol{\kappa}^{\mathrm{s}} \cdot \mathbf{l}^{\mathrm{s}} - \mathrm{v}^{\mathrm{s}}\boldsymbol{\kappa}^{\mathrm{s}} \cdot \mathbf{d}^{\mathrm{s}} \\ \mathrm{v}^{\mathrm{s}}\rho^{\mathrm{s}} \\ -\mathrm{v}^{\mathrm{s}}\rho^{\mathrm{s}} \\ \frac{\mathrm{v}^{\mathrm{s}}\mathrm{q}^{\mathrm{s}}}{\rho^{\mathrm{s}}}\left(-\boldsymbol{\kappa}^{\mathrm{s}} \cdot \mathbf{l}^{\mathrm{s}} + \boldsymbol{\kappa}^{\mathrm{s}} \cdot \mathbf{d}^{\mathrm{s}}\right) \end{bmatrix}, \quad \mathbf{S}(\mathbf{Q}) = \begin{bmatrix} \mathrm{v}^{\mathrm{s}}\mathrm{q}^{\mathrm{s}} \\ 0 \\ 0 \\ \mathbf{A}^{\mathrm{s}}\Delta\mathrm{v}^{\mathrm{s}} \end{bmatrix}. \quad (16)$$

By decomposing the flux direction of Eq. (15) into the components along $\mathbf{d}^{\mathrm{s}}$ and $\mathbf{l}^{\mathrm{s}}$, we can rewrite Eq. (15) as

$$\partial_{\mathrm{t}}\mathbf{Q} + \left[\nabla_{\mathbf{l}^{\mathrm{s}}}\mathbf{F}(\mathbf{Q})\right]\mathbf{l}^{\mathrm{s}} + \left[\nabla_{\mathbf{d}^{\mathrm{s}}}\mathbf{F}(\mathbf{Q})\right]\mathbf{d}^{\mathrm{s}} = \mathbf{S}(\mathbf{Q}), \quad (17)$$

where $\nabla_{\mathbf{l}^{\mathrm{s}}}\mathbf{F}(\mathbf{Q}) = \nabla\mathbf{F}(\mathbf{Q}) \cdot \mathbf{l}^{\mathrm{s}}$ and $\nabla_{\mathbf{d}^{\mathrm{s}}}\mathbf{F}(\mathbf{Q}) = \nabla\mathbf{F}(\mathbf{Q}) \cdot \mathbf{d}^{\mathrm{s}}$.

In the domain of a finite element cell Ω with the boundary (faces) $\partial\Omega$ of each cell, integration by parts yields the corresponding weak formulation

$$\int_{\Omega} \partial_{\mathrm{t}}\mathbf{Q}\Psi\, dV + \sum_{\text{faces}} \int_{\partial\Omega} \mathbf{N} \cdot \mathbf{F}^*(\mathbf{Q})\Psi\, dA - \int_{\Omega} \mathbf{F}(\mathbf{Q})\nabla\Psi\, dV = \int_{\Omega} \mathbf{S}\Psi\, dV, \quad (18)$$

where Ψ are smooth test functions with sufficient continuity, $\mathbf{F}^*$ represents the numerical flux on $\partial\Omega$, V and A indicate the volume and surface area of cell Ω, and $\mathbf{N}$ is the face normal on $\partial\Omega$.

We now describe the choice of the numerical flux functions $\mathbf{F}^*$ required for the discontinuous Galerkin scheme to solve the PDEs of the CDD problem. The CDD problem can be re-written as a quasi-linear form as

$$\partial_{\mathrm{t}}\mathbf{Q} + \mathbf{J}(\mathbf{Q})\nabla\mathbf{Q} = \mathbf{S}(\mathbf{Q}), \quad \mathbf{J}(\mathbf{Q}) = \frac{\partial\mathbf{F}(\mathbf{Q})}{\partial\mathbf{Q}}, \quad (19)$$

where $\mathbf{J}(\mathbf{Q})$ is the Jacobian matrix

$$\mathbf{J}(\mathbf{Q}) = \begin{bmatrix} 0 & \mathrm{v}^{\mathrm{s}} & -\mathrm{v}^{\mathrm{s}} & 0 \\ \mathrm{v}^{\mathrm{s}} & 0 & 0 & 0 \\ -\mathrm{v}^{\mathrm{s}} & 0 & 0 & 0 \\ 0 & 0 & 0 & \frac{\mathrm{v}^{\mathrm{s}}}{\rho^{\mathrm{s}}}\left(-\boldsymbol{\kappa}^{\mathrm{s}} \cdot \mathbf{l}^{\mathrm{s}} + \boldsymbol{\kappa}^{\mathrm{s}} \cdot \mathbf{d}^{\mathrm{s}}\right) \end{bmatrix}. \quad (20)$$

By decomposing the quasi-linear form (Eq. (19)) along the directions of $\mathbf{d}^{\mathrm{s}}$ and $\mathbf{l}^{\mathrm{s}}$, we obtain the following expression

$$\partial_{\mathrm{t}}\mathbf{Q} + \mathbf{J}_{\mathbf{l}^{\mathrm{s}}}\left(\mathbf{Q}_{\mathbf{l}^{\mathrm{s}}}\right)\left[\nabla_{\mathbf{l}^{\mathrm{s}}}\left(\mathbf{Q}_{\mathbf{l}^{\mathrm{s}}}\right)\right] + \mathbf{J}_{\mathbf{d}^{\mathrm{s}}}\left(\mathbf{Q}_{\mathbf{d}^{\mathrm{s}}}\right)\left[\nabla_{\mathbf{d}^{\mathrm{s}}}\left(\mathbf{Q}_{\mathbf{d}^{\mathrm{s}}}\right)\right] = \mathbf{S}(\mathbf{Q}), \quad (21)$$

and

$$\mathbf{J}_{\mathbf{l}^{\mathrm{s}}} = \begin{bmatrix} 0 & \mathrm{v}^{\mathrm{s}} & 0 \\ \mathrm{v}^{\mathrm{s}} & 0 & 0 \\ 0 & 0 & \frac{\mathrm{v}^{\mathrm{s}}}{\rho^{\mathrm{s}}}\left(-\boldsymbol{\kappa}^{\mathrm{s}} \cdot \mathbf{l}^{\mathrm{s}}\right) \end{bmatrix}, \quad \mathbf{J}_{\mathbf{d}^{\mathrm{s}}} = \begin{bmatrix} 0 & -\mathrm{v}^{\mathrm{s}} & 0 \\ -\mathrm{v}^{\mathrm{s}} & 0 & 0 \\ 0 & 0 & \frac{\mathrm{v}^{\mathrm{s}}}{\rho^{\mathrm{s}}}\left(\boldsymbol{\kappa}^{\mathrm{s}} \cdot \mathbf{d}^{\mathrm{s}}\right) \end{bmatrix},$$

$$\mathbf{Q}_{\mathbf{l}^{\mathrm{s}}} = \begin{bmatrix} \rho^{\mathrm{s}} \\ \boldsymbol{\kappa}^{\mathrm{s}} \cdot \mathbf{l}^{\mathrm{s}} \\ \mathrm{q}^{\mathrm{s}} \end{bmatrix}, \quad \mathbf{Q}_{\mathbf{d}^{\mathrm{s}}} = \begin{bmatrix} \rho^{\mathrm{s}} \\ \boldsymbol{\kappa}^{\mathrm{s}} \cdot \mathbf{d}^{\mathrm{s}} \\ \mathrm{q}^{\mathrm{s}} \end{bmatrix}. \quad (22)$$

The eigenvalues of both $\mathbf{J}_{\mathbf{l}^{\mathrm{s}}}$ and $\mathbf{J}_{\mathbf{d}^{\mathrm{s}}}$ are denoted as $\lambda^{(\ell)}_{\mathbf{l}^{\mathrm{s}}}$ and $\lambda^{(\ell)}_{\mathbf{d}^{\mathrm{s}}}$

$$\lambda^{(1)}_{\mathbf{l}^{\mathrm{s}}} = \frac{\mathrm{v}^{\mathrm{s}}}{\rho^{\mathrm{s}}}\left(-\boldsymbol{\kappa}^{\mathrm{s}} \cdot \mathbf{l}^{\mathrm{s}}\right), \quad \lambda^{(1)}_{\mathbf{d}^{\mathrm{s}}} = \frac{\mathrm{v}^{\mathrm{s}}}{\rho^{\mathrm{s}}}\left(\boldsymbol{\kappa}^{\mathrm{s}} \cdot \mathbf{d}^{\mathrm{s}}\right), \quad \lambda^{(2)}_{\mathbf{l}^{\mathrm{s}}} = \lambda^{(2)}_{\mathbf{d}^{\mathrm{s}}} = -\mathrm{v}^{\mathrm{s}},$$
$$\lambda^{(3)}_{\mathbf{l}^{\mathrm{s}}} = \lambda^{(3)}_{\mathbf{d}^{\mathrm{s}}} = \mathrm{v}^{\mathrm{s}}. \quad (23)$$

The corresponding eigenvectors for the directions $\mathbf{l}^{\mathrm{s}}$ and $\mathbf{d}^{\mathrm{s}}$ are denoted as $\mathbf{K}^{(\ell)}_{\mathbf{l}^{\mathrm{s}}}$ and $\mathbf{K}^{(\ell)}_{\mathbf{d}^{\mathrm{s}}}$ respectively. They are

$$\mathbf{K}^{(1)}_{\mathbf{l}^{\mathrm{s}}} = \begin{pmatrix} 0 \\ 0 \\ 1 \end{pmatrix}, \quad \mathbf{K}^{(2)}_{\mathbf{l}^{\mathrm{s}}} = \begin{pmatrix} -1 \\ 1 \\ 0 \end{pmatrix}, \quad \mathbf{K}^{(3)}_{\mathbf{l}^{\mathrm{s}}} = \begin{pmatrix} 1 \\ 1 \\ 0 \end{pmatrix},$$
$$\mathbf{K}^{(1)}_{\mathbf{d}^{\mathrm{s}}} = \begin{pmatrix} 0 \\ 0 \\ 1 \end{pmatrix}, \quad \mathbf{K}^{(2)}_{\mathbf{d}^{\mathrm{s}}} = \begin{pmatrix} 1 \\ 1 \\ 0 \end{pmatrix}, \quad \mathbf{K}^{(3)}_{\mathbf{d}^{\mathrm{s}}} = \begin{pmatrix} -1 \\ 1 \\ 0 \end{pmatrix}. \quad (24)$$

We find that the CDD problem is a linearly degenerate system since for all ℓ along both $\mathbf{l}^{\mathrm{s}}$ and $\mathbf{d}^{\mathrm{s}}$ directions it holds

$$\nabla\lambda^{(\ell)}_{\phi}(\mathbf{Q}) \cdot \mathbf{K}^{(\ell)}_{\phi}(\mathbf{Q}) = 0, \quad \forall\mathbf{Q} \quad \text{and} \quad \phi = \{\mathbf{l}^{\mathrm{s}}, \mathbf{d}^{\mathrm{s}}\}. \quad (25)$$

This implies that the characteristic field of the CDD problem always results in a contact discontinuity, with no possibility of shock or rarefaction formation under any conditions. Consequently, the general solution can be obtained without the need to account for shock or rarefaction wave formations [36, Chapter 2.4].

After analyzing the characteristics of the flux, we proceed to derive the numerical flux $\mathbf{F}^*$ for the CDD problem using an upwind numerical method. Note that this is positivity preserving which is an important physical property of the density evolution. The numerical flux on the faces $\partial\Omega$ of an element is computed based on the direction of information propagation within each cell. To determine the upwind flux direction, we apply the Flux Vector Splitting method as described in [36, Chapter 8]. This method simplifies the identification of upwind directions compared to Godunov-type methods, resulting in more straightforward scheme determining the flux direction. We demonstrate the flux direction centered on the cell located at (i, j, k) across the six inner faces at $i \pm \frac{1}{2}$, $j \pm \frac{1}{2}$, and $k \pm \frac{1}{2}$, as depicted in Fig. 1.

For simplicity, we first showcase the flux direction along the x-direction only, as shown in Fig. 1. The flux in the y- and z-directions can be determined analogously. We denote the x-direction net numerical flux originated within cell positioned at (i, j, k) as $\mathbf{F}^*_i$. We can first split $\mathbf{F}^*_i$ into the positive and negative directions as detailed in [36],

$$\mathbf{F}^*_i = \mathbf{F}^{*+}_i + \mathbf{F}^{*-}_i. \quad (26)$$

Then we further decompose $\mathbf{F}^{*+}_i$ and $\mathbf{F}^{*-}_i$ along the directions of $\mathbf{l}^{\mathrm{s}}$ and $\mathbf{d}^{\mathrm{s}}$ as Eq. (21)

$$\mathbf{F}^*_i = \left(\mathbf{F}^{*+}_i\right)_{\mathbf{l}^{\mathrm{s}}} + \left(\mathbf{F}^{*+}_i\right)_{\mathbf{d}^{\mathrm{s}}} + \left(\mathbf{F}^{*-}_i\right)_{\mathbf{l}^{\mathrm{s}}} + \left(\mathbf{F}^{*-}_i\right)_{\mathbf{d}^{\mathrm{s}}}, \quad (27)$$

where

$$\left(\mathbf{F}^{*\alpha}_i\right)_{\phi} = \mathbf{K}_{\phi}\Lambda^{\alpha}_{\phi}\mathbf{K}^{-1}_{\phi} \quad \text{with} \quad \alpha = \{+, -\} \quad \text{and} \quad \phi = \{\mathbf{l}^{\mathrm{s}}, \mathbf{d}^{\mathrm{s}}\}. \quad (28)$$

The eigenvector matrix $\mathbf{K}_{\phi} = [\mathbf{K}^{(1)}_{\phi}, \mathbf{K}^{(2)}_{\phi}, \mathbf{K}^{(3)}_{\phi}]$, and Λ^{α}_{ϕ} are the diagonal matrices of the positive (i.e., $\lambda^{(\ell)+}_{\phi}$) and negative (i.e., $\lambda^{(\ell)-}_{\phi}$) eigenvalues

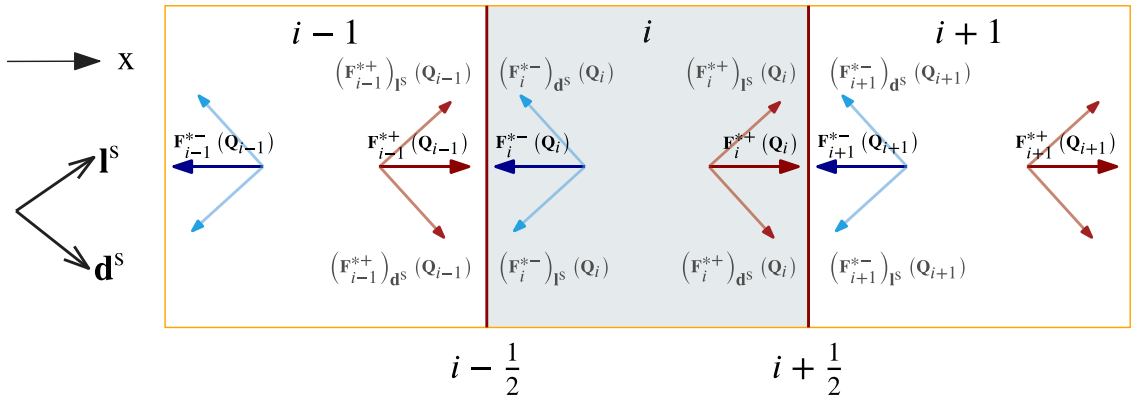

Fig. 1. Illustration of flux splitting at the inner faces along the x-direction. The numerical flux is first split into positive (marked in red) and negative (marked in blue) components, then further decomposed along the line direction $\mathbf{l}^s$ and the slip (Burger's) direction $\mathbf{d}^s$. The contribution terms to the fluxes at the interfaces $i+\frac{1}{2}$ and $i-\frac{1}{2}$ are shown.

along the direction ϕ, and is given by

$$\Lambda_\phi^+ = \begin{bmatrix} \lambda_\phi^{(1)+} & 0 & 0 \\ 0 & \lambda_\phi^{(2)+} & 0 \\ 0 & 0 & \lambda_\phi^{(3)+} \end{bmatrix}, \quad \Lambda_\phi^- = \begin{bmatrix} \lambda_\phi^{(1)-} & 0 & 0 \\ 0 & \lambda_\phi^{(2)-} & 0 \\ 0 & 0 & \lambda_\phi^{(3)-} \end{bmatrix}. \tag{29}$$

For the full upwind flux, the eigenvalues are decomposed into four directions, combining positive/negative contributions and line/Burger's directions, as follows

$$\lambda_\phi^{(\ell)} = \lambda_\phi^{(\ell)+} + \lambda_\phi^{(\ell)-}, \qquad \phi = \{\mathbf{l}^s, \mathbf{d}^s\} \tag{30}$$

such that $\lambda_\phi^{(\ell)+} \geq 0$ and $\lambda_\phi^{(\ell)-} \leq 0$, and the definition for $\lambda_\phi^{(\ell)+}$ and $\lambda_\phi^{(\ell)-}$ are given by

$$\lambda_\phi^{(\ell)+} = \frac{1}{2}(\lambda_\phi^{(\ell)} + |\lambda_\phi^{(\ell)}|), \quad \lambda_\phi^{(\ell)-} = \frac{1}{2}(\lambda_\phi^{(\ell)} - |\lambda_\phi^{(\ell)}|). \tag{31}$$

As illustrated in Fig. 1, the numerical flux on face $i+\frac{1}{2}$ is contributed by the positive flux from cell at position i, denoted as $\mathbf{F}_i^{*+}(\mathbf{Q}_i)$, and the negative flux from cell at position $i+1$, denoted as $\mathbf{F}_{i+1}^{*-}(\mathbf{Q}_{i+1})$. Therefore, the numerical flux on face $i+\frac{1}{2}$ is

$$\begin{aligned} \mathbf{F}_{i+\frac{1}{2}}^* &= \mathbf{F}_i^{*+}(\mathbf{Q}_i) + \mathbf{F}_{i+1}^{*-}(\mathbf{Q}_{i+1}) \\ &= (\mathbf{F}_i^{*+})_{\mathbf{l}^s}(\mathbf{Q}_i) + (\mathbf{F}_i^{*+})_{\mathbf{d}^s}(\mathbf{Q}_i) + (\mathbf{F}_{i+1}^{*-})_{\mathbf{l}^s}(\mathbf{Q}_{i+1}) + (\mathbf{F}_{i+1}^{*-})_{\mathbf{d}^s}(\mathbf{Q}_{i+1}), \end{aligned} \tag{32}$$

similarly, the numerical flux on face $i-\frac{1}{2}$ is

$$\begin{aligned} \mathbf{F}_{i-\frac{1}{2}}^* &= \mathbf{F}_{i-1}^{*+}(\mathbf{Q}_{i-1}) + \mathbf{F}_i^{*-}(\mathbf{Q}_i) \\ &= (\mathbf{F}_i^{*-})_{\mathbf{l}^s}(\mathbf{Q}_i) + (\mathbf{F}_i^{*-})_{\mathbf{d}^s}(\mathbf{Q}_i) + (\mathbf{F}_{i-1}^{*+})_{\mathbf{l}^s}(\mathbf{Q}_{i-1}) + (\mathbf{F}_{i-1}^{*+})_{\mathbf{d}^s}(\mathbf{Q}_{i-1}). \end{aligned} \tag{33}$$

We now analyze the numerical flux in a fully three-dimensional setting. The geometric relationship between the target cell at (i,j,k) and its neighboring cells is depicted in Fig. 2(a). Since there is no out-of-plane dislocation movement, the three-dimensional flux problem can be simplified to the flux on a plane where the normal aligns with the slip plane normal, $\mathbf{n}^s$, shown as the plane in Fig. 2(a). The net numerical flux across the six inner faces ($\partial\Omega$) of the cell positioned at (i,j,k) is depicted in Fig. 2(b). As seen in this figure, the direction for splitting the numerical flux is determined by the face outward normal, $\mathbf{N}_f$, where $f = \{i+\frac{1}{2}, i-\frac{1}{2}, j+\frac{1}{2}, j-\frac{1}{2}, k+\frac{1}{2}, k-\frac{1}{2}\}$ and the directions of $\mathbf{l}^s$ and $\mathbf{d}^s$. This results in the numerical flux on each face being split into four components: combinations of positive/negative and line/Burger's directions, as shown in Eq. (27). Thus, for a hexahedron cell with six faces, the total numerical flux computation involves 24 terms. Consequently, the second term in Eq. (18) is split into 24 terms calculated based on the sign of velocity, $\mathbf{N}_f$, $\mathbf{l}^s$, and $\mathbf{d}^s$ as

$$\begin{aligned} \sum_{\text{face}} \int_{\partial\Omega} \mathbf{N}_f \cdot \mathbf{F}^*(\mathbf{Q}) \Psi \, dA = & \\ - \sum_f \Bigg\{ & \left| \left(\mathbf{F}_i^{*\text{sign}(\mathbf{l}^s \cdot \mathbf{N}_f)} \right)_{\mathbf{l}^s} (\mathbf{Q}_i) \right| |\mathbf{l}^s \cdot \mathbf{N}_f| \\ & + \left| \left(\mathbf{F}_i^{*\text{sign}(\mathbf{d}^s \cdot \mathbf{N}_f)} \right)_{\mathbf{d}^s} (\mathbf{Q}_i) \right| |\mathbf{d}^s \cdot \mathbf{N}_f| \Bigg\} \\ + \sum_{f^+} \Bigg\{ & \left| \left(\mathbf{F}_{f^+ + \frac{1}{2}}^{*\text{sign}(\mathbf{l}^s \cdot -\mathbf{N}_f)} \right)_{\mathbf{l}^s} \left(\mathbf{Q}_{f^+ + \frac{1}{2}} \right) \right| |\mathbf{l}^s \cdot \mathbf{N}_f| \\ & + \left| \left(\mathbf{F}_{f^+ + \frac{1}{2}}^{*\text{sign}(\mathbf{d}^s \cdot -\mathbf{N}_f)} \right)_{\mathbf{d}^s} \left(\mathbf{Q}_{f^+ + \frac{1}{2}} \right) \right| |\mathbf{d}^s \cdot \mathbf{N}_f| \Bigg\} \\ + \sum_{f^-} \Bigg\{ & \left| \left(\mathbf{F}_{f^- - \frac{1}{2}}^{*\text{sign}(\mathbf{l}^s \cdot -\mathbf{N}_f)} \right)_{\mathbf{l}^s} \left(\mathbf{Q}_{f^- - \frac{1}{2}} \right) \right| |\mathbf{l}^s \cdot \mathbf{N}_f| \\ & + \left| \left(\mathbf{F}_{f^- - \frac{1}{2}}^{*\text{sign}(\mathbf{d}^s \cdot -\mathbf{N}_f)} \right)_{\mathbf{d}^s} \left(\mathbf{Q}_{f^- - \frac{1}{2}} \right) \right| |\mathbf{d}^s \cdot \mathbf{N}_f| \Bigg\}, \end{aligned} \tag{34}$$

where $f^+ = \{i+\frac{1}{2}, j+\frac{1}{2}, k+\frac{1}{2}\}$ and $f^- = \{i-\frac{1}{2}, j-\frac{1}{2}, k-\frac{1}{2}\}$.

2.3. Implicit coupling between the macro and micro problems

To couple the macro and the micro problem in our numerical scheme, we develop an implicit coupling method. This approach addresses the limitations of explicit coupling, which restricts the time step size and can lead to inaccuracies or divergence in extensive simulations [35]. By using implicit coupling, we can simulate larger deformations, such as those seen in tribological loading, with improved stability and accuracy.

The implicit-coupling algorithm is shown in Algorithm 1. At each macro time step T_n with step size $\triangle T$, the macro problem is solved using the implicit Euler method to compute the displacement field $\boldsymbol{u}$. The solution $\boldsymbol{u}$ for Eq. (2) is considered converged when the internal force deviates from the external force imposed by the boundary conditions by no more than ξ_{force}.

Using the resulting macro stress field, we proceed to solve the micro (CDD) problem at micro time steps t_m^0 with step size $\triangle t$. For each slip system s, we first compute τ^s (Eq. (10)) and τ_y^s (Eq. (13)) from the macro stress field. Based on these, v^s (Eq. (9)) is computed. Next, the dislocation evolution PDEs (Eq. (7)) rates are solved using a diagonally implicit Runge–Kutta method, followed by updating the plastic slip (Eq. (5)). The τ^s and τ_y^s are then recomputed to check for any overshoot beyond the yield surface. If overshooting occurs, the micro time step is

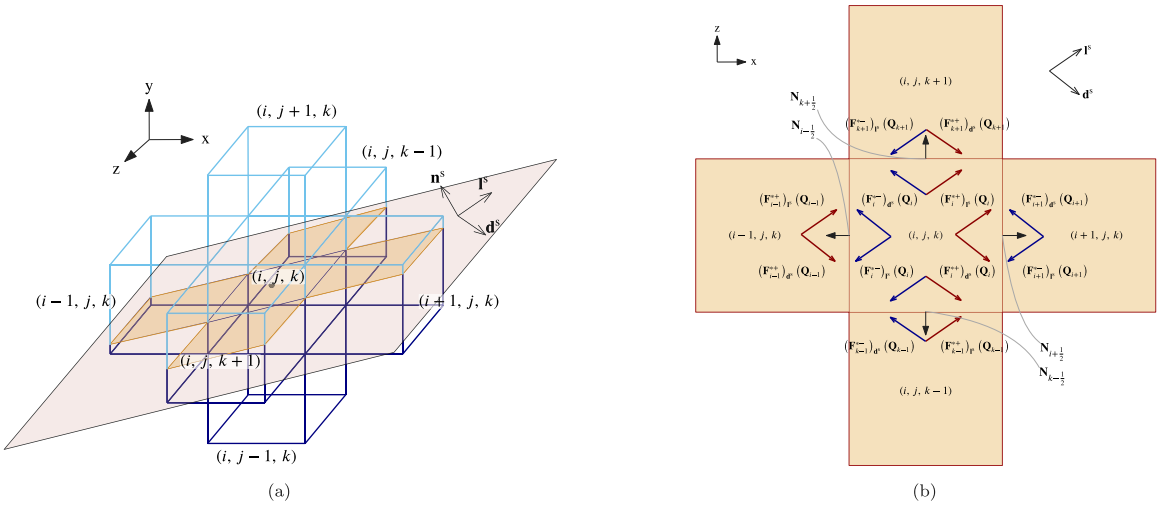

Fig. 2. Geometric relationship between the target cell at (i, j, k) and its neighboring cells, highlighting the alignment of the slip plane, and their relationship to the line direction $\mathbf{l}^s$, and the slip (Burgers) direction $\mathbf{d}^s$. (a) 3D representation of the target cell at (i, j, k) and the slip plane, where the net numerical flux is plotted. (b) Visualization of the net numerical flux on the slip plane $\mathbf{n}^s$, with flux splitting determined by the face outward normal $\mathbf{N}_f$, the line direction $\mathbf{l}^s$, and the slip direction $\mathbf{d}^s$.

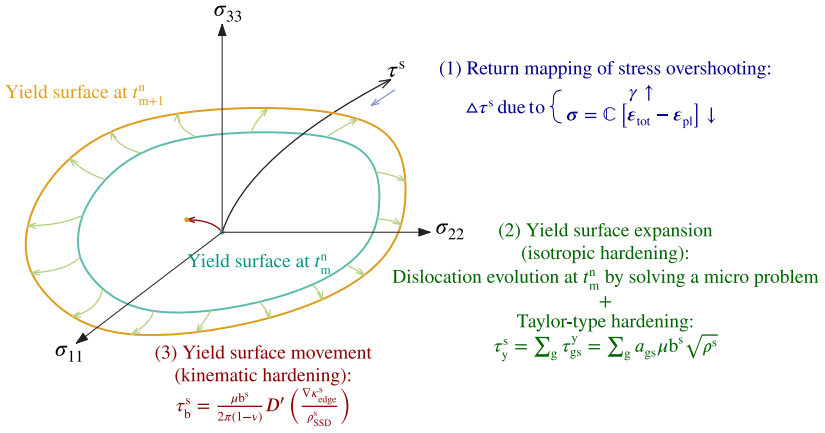

Fig. 3. Illustration of the correction process for overshooting outside the yield surface in relation to dislocation dynamics over each micro time step.

repeated (i.e., $t^2_m, \ldots, t^n_m$) until τ^s returns to the yield surface τ^s_y within a tolerance ξ_y, or the micro time series reaches the next macro time step.

The computation in the micro time series is served as a micro iteration for the implicit coupling algorithm. And for each micro time step calculation, there are three mechanisms narrowing the gap between τ^s and τ^s_y, as shown in Fig. 3. First, plastic slip increases after each micro time step Δt, driven by dislocation kinematics. The slip increment, calculated using Eq. (5), represents the swept area by dislocations within Δt, reducing the stress state via microstructure relaxation and mapping τ^s back onto the yield surface (blue arrow in Fig. 3). Second, isotropic hardening arises from microstructural evolution and dislocation reactions across slip systems (latent hardening) within Δt, expanding the yield surface via a Taylor-type model in the Franciosi's formulation (green arrow in Fig. 3). Finally, kinematic hardening results from dislocation heterogeneity under the numerical discretization scale, shifting the yield surface (red arrow in Fig. 3).

2.4. Boundary condition for simulating contact problems

To simulate tribological loading, we model a force-controlled contact problem by applying Neumann boundary conditions along with a penalty contact criterion. This approach calculates the interaction between the deformable material and a rigid, analytically defined spherical indenter. The system setup is illustrated in Fig. 4(a). The indenter is characterized by its center coordinates, $\mathbf{C}_{indent}$, and radius, R_{indent}. The indented material is a rectangular box with dimensions L_x, L_y, and L_z, with the contact surface, Γ_c, highlighted in yellow in Fig. 4(a).

The iterative algorithm for computing contact interactions is outlined in Algorithm 2. At the beginning of each macro time step T_n, initialization is performed: the applied force, $\mathcal{F}_{applied}$, is predefined as a function of T_n, while the penalty force, $\mathcal{F}_{penalty}$, is initially set to zero. And the net force applied on the indenter, $\mathcal{F}_{net} = \mathcal{F}_{penalty} - \mathcal{F}_{applied}$.

After initialization, the iteration proceeds in three main steps: updating the indenter's position, evaluating the gap function $\mathcal{G}(\mathbf{x})$ at each node $\mathbf{x}$ on Γ_c, and updating $\mathcal{F}_{penalty}$ and $\mathcal{F}_{net}$. This process is repeated until $\mathcal{F}_{net}$ falls within the tolerance threshold, ξ_{indent}.

To update the indenter's position, the net force on the indenter, $\mathcal{F}_{net} = \mathcal{F}_{penalty} - \mathcal{F}_{applied}$, is first computed. $\mathbf{C}_{indent}$ is then updated as

$$\mathbf{C}_{indent} := \mathbf{C}_{indent} + \frac{\mathcal{F}_{net}}{M_{indent}}, \tag{35}$$

where M_{indent} is the iteration scaling factor for contact search.

Evaluating $\mathcal{G}(\mathbf{x})$ at each node $\mathbf{x}$ on Γ_c consists of two steps, as illustrated in Fig. 4(b). First, the projected point $\mathbf{x}_{projected}$, representing the projection of $\mathbf{x}$ onto the indenter, is computed. Then, the penetration is assessed. Penetration occurs at $\mathbf{x}$ if the inner product between $(\mathbf{x} - \mathbf{x}_{projected})$ and $(\mathbf{C}_{indent} - \mathbf{x}_{projected})$ is positive, indicating that the

Algorithm 1 Algorithm for the implicit-coupled elastoplasticity model.

Input: Dirichlet boundary condition $\boldsymbol{u}_{\mathrm{D}}$ or the Neumann boundary condition $\boldsymbol{t}_{\mathrm{S}}$ at time T_{n} for Equation (3) for each $\mathrm{n} \leqq \mathrm{N}$ to solve the macro problem.

Input: Initial condition for $\left[\rho^{\mathrm{s}}, \boldsymbol{\kappa}^{\mathrm{s}} \cdot \mathbf{l}^{\mathrm{s}}, \boldsymbol{\kappa}^{\mathrm{s}} \cdot \mathbf{d}^{\mathrm{s}}, \mathrm{q}^{\mathrm{s}}\right]$ are specified for all slip systems s and all elements at $T = 0$ to solve the micro problem.

1: **for** $n = 0, \ldots, \mathrm{N}$ **do**

2: Initialize macro problem:
$T \Leftarrow \mathrm{n}\triangle T$, $t \Leftarrow t_1^{\mathrm{n}}$, and $\boldsymbol{u} \Leftarrow \boldsymbol{u}_{\mathrm{D}}(T)$ or $\boldsymbol{\sigma} \cdot \boldsymbol{n}_{\partial\mathcal{B}} \Leftarrow \boldsymbol{t}_{\mathrm{S}}(T)$, $\mathrm{m} = 1$.

3: **repeat**

4: Update plastic deformation based on the plastic slip of each slip system:
$\boldsymbol{\epsilon}_{\mathrm{pl}}(T) \Leftarrow \mathrm{sym}\left(\sum_{\mathrm{s}=1}^{12} \gamma^{\mathrm{s}}(t)\, \mathbf{M}^{\mathrm{s}}\right)$.

5: Solve macro problem for $\boldsymbol{u}$ to achieve force balance (implicit Euler):
5.1 update stress state $\boldsymbol{\sigma}(T) \Leftarrow \mathbb{C}\left[\boldsymbol{\epsilon}_{\mathrm{tot}}(T) - \boldsymbol{\epsilon}_{\mathrm{pl}}(T)\right]$.
5.2 find $\boldsymbol{u}$ that satisfies $\|\boldsymbol{f}_{\mathcal{B}} + \nabla\boldsymbol{\sigma}(T)\| \leq \xi_{\mathrm{force}}$ (Equation (2)).

6: **for all** slip system s **do**

7: Update dislocation velocity:
7.1 calculate τ^{s} from Equation (10) and $\tau_{\mathrm{y}}^{\mathrm{s}}$ from Equation (13).
7.2 **if** $|\tau^{\mathrm{s}}| > \tau_{\mathrm{y}}^{\mathrm{s}}$
$\mathrm{v}^{\mathrm{s}}(t) \Leftarrow \frac{\mathrm{b}^{\mathrm{s}}}{\mathrm{B}}(|\tau^{\mathrm{s}}| - \tau_{\mathrm{y}}^{\mathrm{s}})\,\mathrm{sign}(\tau^{\mathrm{s}})$
else
$\mathrm{v}^{\mathrm{s}}(t) \Leftarrow 0$.

8: **if** $\mathrm{v}^{\mathrm{s}}(t) \neq 0$ **then**

9: Solve micro (CDD) problem (implicit RK):
compute $\partial_t\rho^{\mathrm{s}}$, $\partial_t\boldsymbol{\kappa}^{\mathrm{s}}$, and $\partial_t\mathrm{q}^{\mathrm{s}}$ by solving Equation (7).

10: Update microstructure:
$\rho^{\mathrm{s}}(t) \Leftarrow \rho^{\mathrm{s}}(t_{\mathrm{old}}) + \partial_t\rho^{\mathrm{s}} \cdot \triangle t$, $\boldsymbol{\kappa}^{\mathrm{s}}(t) \Leftarrow \boldsymbol{\kappa}^{\mathrm{s}}(t_{\mathrm{old}}) + \partial_t\boldsymbol{\kappa}^{\mathrm{s}} \cdot \triangle t$, $\mathrm{q}^{\mathrm{s}}(t) \Leftarrow \mathrm{q}^{\mathrm{s}}(t_{\mathrm{old}}) + \partial_t\mathrm{q}^{\mathrm{s}} \cdot \triangle t$

11: Evaluate plastic slip:
$\partial_t\gamma^{\mathrm{s}}(t) \Leftarrow \mathrm{v}^{\mathrm{s}}(t)\mathrm{b}^{\mathrm{s}}\rho^{\mathrm{s}}(t)$ (Equation (5))

12: Evaluate resolved shear stress:
update τ^{s} from Equation (10) and $\tau_{\mathrm{y}}^{\mathrm{s}}$ from Equation (13).

13: $t_{\mathrm{old}} = t$ and $\mathrm{m} := \mathrm{m} + 1$

14: **until** $\max(|\tau^{\mathrm{s}} - \tau_{\mathrm{y}}^{\mathrm{s}}|) \leq \xi_{\mathrm{y}}$ or $\mathrm{m} = \mathrm{M}$

15: $\mathrm{n} := \mathrm{n} + 1$

Output: The displacement field $\boldsymbol{u}$ at each time step T influenced by external loading and microstructure evolution.

Output: Dislocation densities evolution $\left[\rho^{\mathrm{s}}, \boldsymbol{\kappa}^{\mathrm{s}} \cdot \mathbf{l}^{\mathrm{s}}, \boldsymbol{\kappa}^{\mathrm{s}} \cdot \mathbf{d}^{\mathrm{s}}, \mathrm{q}^{\mathrm{s}}\right]$ for all slip systems s at each time step t.

angle between the two vectors is less than 90°. In this case, $\mathcal{G}(\mathbf{x})$ is defined as

$$\mathcal{G}(\mathbf{x}) = \mathbf{x} - \mathbf{x}_{\mathrm{projected}}. \tag{36}$$

If the inner product is zero or negative, penetration does not occur. We then set $\mathcal{G}(\mathbf{x})$ to be a zero vector.

Once the penetration criterion has been evaluated for all nodes on Γ_c, the penalty force $\mathcal{F}_{\mathrm{penalty}}$ is updated as the sum of the gap function over Γ_c, weighted by the penalty parameter ω_0, such that

$$\mathcal{F}_{\mathrm{penalty}} = \sum_{\Gamma_c} \omega_0 \mathcal{G}(\mathbf{x}). \tag{37}$$

In the end, we update the $\mathcal{F}_{\mathrm{net}}$ on the indentaer as the difference between $\mathcal{F}_{\mathrm{applied}}$ and $\mathcal{F}_{\mathrm{penalty}}$. If $\mathcal{F}_{\mathrm{net}}$ falls within a tolerance ξ_{indent}, as illustrated in Fig. 4(c), the Neumann boundary condition (Eq. (3b)) is updated as

$$\boldsymbol{\sigma} \cdot \boldsymbol{n}_{\partial\mathcal{B}} = \boldsymbol{t}_{\mathrm{N}} = -\omega_0 \mathcal{G}(\mathbf{x}), \tag{38}$$

where $\boldsymbol{t}_{\mathrm{N}}$ denoted the normal traction, which is always normal to the indenter surface. Then we start to solve the macro problem (as shown in Step 3 in Algorithm 1).

If $\mathcal{F}_{\mathrm{net}}$ does not fall within a tolerance ξ_{indent}, the indenter's position is further updated, and the process is repeated until the tolerance level ξ_{indent} is reached. As a result, the applied force $\mathcal{F}_{\mathrm{applied}}$ is distributed onto the material as a Neumann boundary condition, while the force exerted on the indenter is simultaneously balanced by the penalty force. To demonstrate the numerical stability, a convergence test for the contact boundary condition has been conducted, as detailed in Appendix A.2.

2.5. Boundary condition for simulating tribological problems

The boundary conditions for simulating a tribological contact problem can be assumed the same as described in Section 2.4, with the center of the indenter, $\mathbf{C}_{\mathrm{indent}}$, slides along the x-direction at a speed of

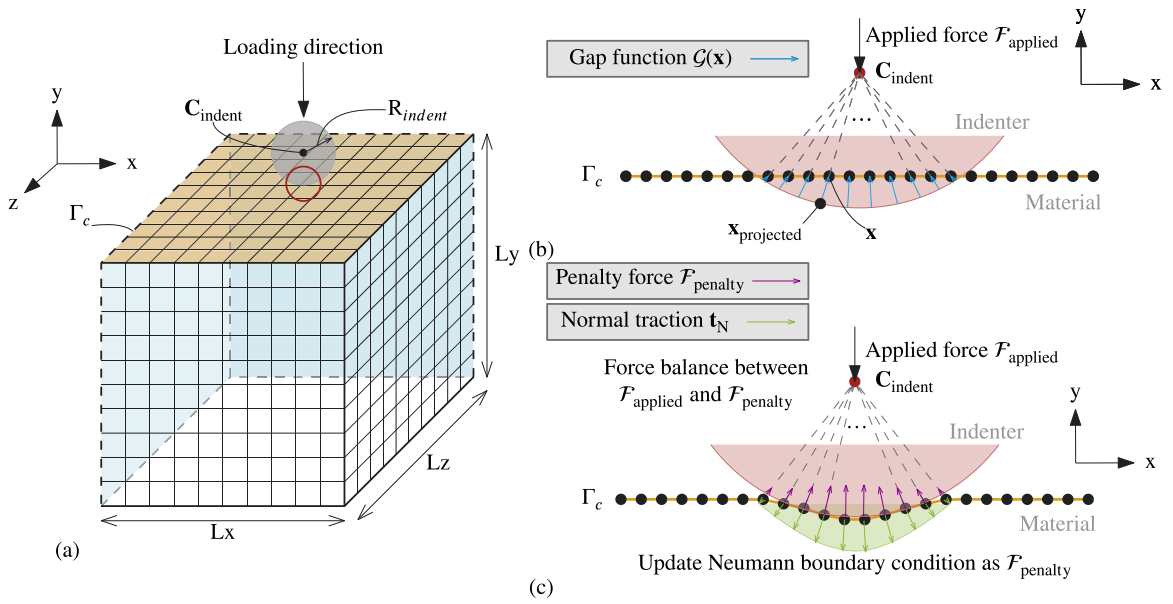

Fig. 4. Contact boundary condition. (a) 3D geometry representation of the material with an indenter contacting at the top surface Γ_c. (b) Illustration of the penetration condition, introducing a gap function $\mathcal{G}(\mathbf{x})$ between the indenter and Γ_c. (c) Upon achieving convergence, the penalty force $\mathcal{F}_{\text{penalty}}$ balances with the applied force $\mathcal{F}_{\text{applied}}$ determining the equilibrium position of the indenter and allowing the Neumann boundary Γ_c to be updated using the value of $\mathcal{F}_{\text{penalty}}$.

Algorithm 2 Algorithm using Neumann boundary condition combined with a penalty contact criterion.

Input: T, $\mathcal{F}_{\text{applied}}(T)$, $\mathbf{C}_{\text{indent}}(T)$.

Initialize contact module:
$\mathcal{F}_{\text{applied}} \Leftarrow \mathcal{F}_{\text{applied}}(T)$, $\mathbf{C}_{\text{indent}} \Leftarrow \mathbf{C}_{\text{indent}}(T)$, $\mathcal{F}_{\text{penalty}} \Leftarrow 0$, $\mathcal{F}_{\text{net}} \Leftarrow \mathcal{F}_{\text{penalty}} - \mathcal{F}_{\text{applied}}$

repeat

  Update the position of the indenter:
  $\mathbf{C}_{\text{indent}} \Leftarrow \mathbf{C}_{\text{indent}} + \frac{\mathcal{F}_{\text{net}}}{\text{M}_{\text{indent}}}$

  for all $\mathbf{x} \in \Gamma_c$ **do**

    Evaluate $\mathcal{G}(\mathbf{x})$:
    5.1 calculate the projected point $\mathbf{x}_{\text{projected}} \Leftarrow \text{R}_{indent} \cdot \frac{\mathbf{x}-\mathbf{C}_{\text{indent}}}{\|\mathbf{x}-\mathbf{C}_{\text{indent}}\|} + \mathbf{C}_{\text{indent}}$
    5.2 **if** $(\mathbf{x} - \mathbf{x}_{\text{projected}}) \cdot (\mathbf{C}_{\text{indent}} - \mathbf{x}_{\text{projected}}) > 0$
      penetration occur, $\mathcal{G}(\mathbf{x}) \Leftarrow \mathbf{x} - \mathbf{x}_{\text{projected}}$
    else
      penetration not occur, $\mathcal{G}(\mathbf{x}) \Leftarrow 0$

  Update $\mathcal{F}_{\text{penalty}}$ and $\mathcal{F}_{\text{net}}$ for the indenter:
  $\mathcal{F}_{\text{penalty}} \Leftarrow \sum_{\Gamma_c} \omega_0 \mathcal{G}(\mathbf{x})$ for all $\mathbf{x}$ on Γ_c
  $\mathcal{F}_{\text{net}} = \mathcal{F}_{\text{penalty}} - \mathcal{F}_{\text{applied}}$

until $|\mathcal{F}_{\text{net}}| \le \xi_{\text{indent}}$

Update the Neumann boundary condition:
$\boldsymbol{t}_{\text{S}} \Leftarrow \boldsymbol{t}_{\text{N}} = -\omega_0 \mathcal{G}(\mathbf{x})$

Output: The Neumann boundary condition induced by contact and continue on Step 3 in Algorithm 1.

v_{slid}. Accordingly, $\mathbf{C}_{\text{indent}}$ is initialized as $\mathbf{C}_{\text{indent}} := \mathbf{C}_{\text{indent}} + \triangle \text{x}_{\text{indent}}$ at the beginning of each macro time step T_{n}.

$$\triangle \text{x}_{\text{indent}} = \left(\text{v}_{\text{slid}} \triangle T\right) \mathbf{d}_{\text{indent}}, \tag{39}$$

where $\mathbf{d}_{\text{indent}}$ is the sliding direction of the indenter it is defined as

$$\mathbf{d}_{\text{indent}} = \begin{cases} (1,\,0,\,0)\,, & \frac{\text{v}_{\text{slid}} T}{\text{L}_{\text{stroke}}} \equiv 0 \pmod 2 \\ (-1,\,0,\,0)\,, & \frac{\text{v}_{\text{slid}} T}{\text{L}_{\text{stroke}}} \equiv 1 \pmod 2 \end{cases} \tag{40}$$

L_{stroke} is the stroke length of sliding. To model frictional forces, a frictional traction $\boldsymbol{t}_{\text{F}}$ is superposed on the normal traction $\boldsymbol{t}_{\text{N}}$ calculated in Eq. (38). A Coulomb friction model is employed to compute $\boldsymbol{t}_{\text{F}}$, introducing a tangential traction proportional to $\boldsymbol{t}_{\text{N}}$, scaled by the friction coefficient μ_{friction}.

The direction of $\boldsymbol{t}_{\text{F}}$ is tangential to the surface normal of the indenter and depends on the sliding direction, making it path-dependent. Specifically, the direction of $\boldsymbol{t}_{\text{F}}$ is defined as the inverse of the projection of $\mathbf{d}_{\text{indent}}$ onto the plane orthogonal to $\boldsymbol{t}_{\text{N}}$. Therefore, $\boldsymbol{t}_{\text{F}}$ is expressed as

$$\boldsymbol{t}_{\text{F}} = -\mu_{\text{friction}} |\boldsymbol{t}_{\text{N}}| \left[\mathbf{d}_{\text{indent}} - \left(\mathbf{d}_{\text{indent}} \cdot \frac{\boldsymbol{t}_{\text{N}}}{|\boldsymbol{t}_{\text{N}}|} \right) \frac{\boldsymbol{t}_{\text{N}}}{|\boldsymbol{t}_{\text{N}}|} \right]. \tag{41}$$

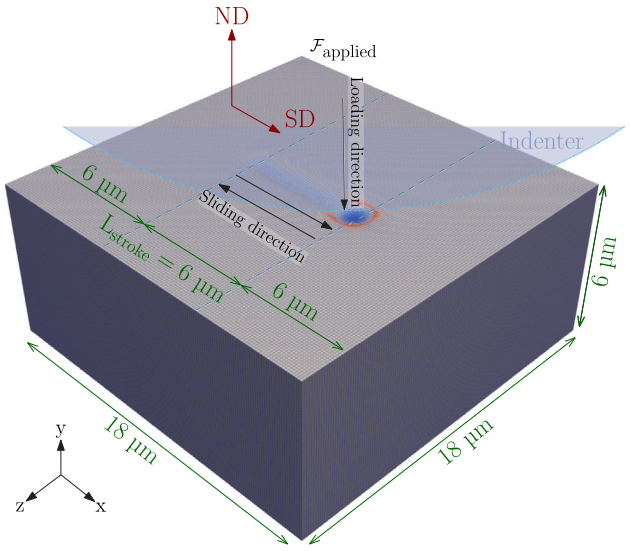

Fig. 5. Simulation setup for a tribological problem. Black arrows indicate the loading and sliding direction of the indenter under global coordinate, red arrows represent the crystal orientation of the material, and green arrows denote the material dimensions. ND refers to the crystal normal direction aligned with the global loading direction, and SD refers to the crystal direction aligned with the global sliding direction.

To sum up, in order to simulate tribological loading together with the effect of frictional force, the Neumann boundary condition (Eq. (3b)) on the material is updated as

$$\boldsymbol{\sigma} \cdot \boldsymbol{n}_{\partial\mathcal{B}} = \boldsymbol{t}_{\text{N}} + \boldsymbol{t}_{\text{F}}, \tag{42}$$

where $\boldsymbol{t}_{\text{N}}$ is the same as Eq. (38) induced by $\mathcal{F}_{\text{applied}}$, and $\boldsymbol{t}_{\text{F}}$ is calculated by Eq. (41) resulting from both $\boldsymbol{t}_{\text{N}}$ and the sliding direction.

2.6. System setup simulating a tribological problem

A detailed overview on material parameters and numerical parameters used in the simulations is listed in Table 3.

We apply the tribological contact boundary condition on a single crystalline copper sample. The material parameters include the isotropic elastic constants $\mu = 40$ GPa and $\nu = 0.367$ and the anisotropic elastic constants $\mathbb{C}_{1111} = 168$ GPa, $\mathbb{C}_{1122} = 121$ GPa, and $\mathbb{C}_{2323} = 75$ GPa. For the micro problem, the drag coefficient $\text{B} = 5 \times 10^{-5}$ sPa is used as specified in Eq. (9). The coefficients of the latent hardening matrix used in Eq. (13) follow the parameters in [37] and are listed in Table 3.

The simulation setup for the considered tribological system is depicted in Fig. 5. For this simulation, the indenter radius R_{indent} is set to 20 μm with an initial position $\mathbf{C}_{\text{indent}} = (9, 26, 9)$ μm. The applied force remains constant throughout the sliding process, $\mathcal{F}_{\text{applied}} = 1$ mN. The stroke length L_{stroke} is 6 μm, and the sliding speed v_{slid} is 15 mm/s. The material dimensions are $\text{L}_x \times \text{L}_y \times \text{L}_z = 18 \times 6 \times 18$ μm, with an initial mobile dislocation density $\rho = 1\,\mu\text{m}^{-2}$ across all 12 slip systems. The selected loading and material parameters result in a Hertzian contact radius 0.5 μm, an elastic imprint depth of 0.3 μm, a maximum Hertzian pressure of 1.6 GPa, and a maximum elastic shear stress of 522 MPa.

The numerical parameters for the contact boundary condition are set as follows: The iteration scaling factor M_{indent} is chosen to be 26500, and the penalty parameter ω_0 is set to 5.0 mN/μm.

The force tolerance ξ_{indent} is selected to be 1×10^{-6} mN. The friction coefficient μ_{friction} is chosen to be 0.25 following the experimental study [6].

The 12 slip systems of FCC crystals considered in this study are listed in Table 1. To investigate the effect of crystal orientation, the crystal coordinate system is adjusted relative to the global coordinate system. In Fig. 5, red arrows indicate the crystal coordinate system, while black arrows represent the global coordinate system. In this context, ND refers to the crystal 'normal' direction aligned with the global loading direction, and SD refers to the crystal direction aligned with the global sliding direction.

Table 1
Notation of the 12 FCC slip systems according to the Schmid & Boas notation.

Slip system (s)	A4	A5	A2	B3	B6	B2
Plane normal $\mathbf{m}^s$	(111)	(111)	(111)	$(11\bar{1})$	$(11\bar{1})$	$(11\bar{1})$
Slip direction $\mathbf{d}^s$	$[01\bar{1}]$	$[10\bar{1}]$	$[\bar{1}10]$	[011]	[101]	$[\bar{1}10]$
Slip system (s)	C4	C6	C1	D3	D5	D1
Plane normal $\mathbf{m}^s$	$(\bar{1}11)$	$(\bar{1}11)$	$(\bar{1}11)$	$(1\bar{1}1)$	$(1\bar{1}1)$	$(1\bar{1}1)$
Slip direction $\mathbf{d}^s$	$[0\bar{1}1]$	[101]	[110]	[011]	$[10\bar{1}]$	[110]

Table 2
Crystal orientation setup for tribological problem.

Setup name	ND	SD
111_{A}	(111)	$[\bar{2}11]$
111_{B}	(111)	$[\bar{1}01]$
010_{A}	(010)	[100]
010_{B}	(010)	[101]

The setups for four crystal orientations analyzed in this study are detailed in Table 2. The setup names are based on the normal direction of the indented surface, with subscripts A and B indicating different sliding directions. The associated Thompson tetrahedron corresponding to the crystal coordinates are shown in Fig. 6.

Regarding the numerical discretization scheme, hexahedral elements with dimensions of $0.125 \times 0.0625 \times 0.125$ μm are applied for both the macro and micro problems simulating the tribological system based on the results from convergence tests in Appendices A.1 and A.2. We subdivide the dimensions of the element along the y-axis to achieve a better resolution along the loading direction for observing the dislocation features beneath the surface. The macro problem employs Lagrange discretization with polynomial degree equal to one, while the micro problem utilizes discontinuous Galerkin discretization with polynomial degree equal to zero (finite volume). The simulation results in this study represent sliding with varying stroke counts, as specified in Section 3. Data was extracted after the material was unloaded and had undergone adequate relaxation periods. For each stroke, we have discretized the macro time domain with $\text{N} = 120$ and micro time domain with $\text{M} = 100$. Both the macro- and micro-scale time steps were selected based on numerical stability constraints and convergence behavior observed in preliminary simulations. ξ_{force} is chosen to be 1×10^{-6} mN and ξ_{y} is chosen to be 1×10^{-6} GPa.

Regarding the computational resources used in this study, we utilized 256 CPU cores and 46 GB peak memory usage calculating two sliding strokes within approximately 23 h.

3. Results

To validate the simulation results, we first compare the numerical predictions with experimental measurements using nano-indentation as a benchmark. We then present results under tribological loading. At the micro-scale, we examine dislocation accumulation, with a focus on the formation of dislocation trace lines and dislocation transport processes. At the macro-scale, we analyze plastic deformation, emphasizing both symmetrical and asymmetrical surface topographies along sliding grooves, the influence of frictional forces under varying crystallographic orientations, and the evolution of the contact area during sliding.

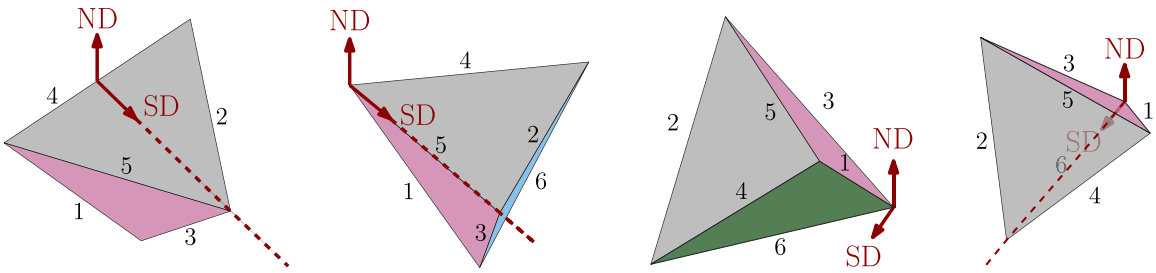

(a) 111_A (b) 111_B (c) 010_A (d) 010_B

Fig. 6. Thompson tetrahedron illustrating the four crystal orientation setups. The color coding represents the plane normal directions: gray for (111), blue for $(11\bar{1})$, green for $(\bar{1}11)$, and pink for $(1\bar{1}1)$.

Table 3
Material, tribological loading, and numerical parameters used in the simulations.

Parameter	Value	Parameter	Value
Material parameters			
$\mathbb{C}_{1111}$, $\mathbb{C}_{1122}$, $\mathbb{C}_{2323}$	168, 121, 75 GPa [38]	ν	0.367 [39]
μ	40 GPa [39]	b^s (for all s)	0.286 nm [40]
B	5×10^{-5} sPa [41]	a_{self}	0.122 [37]
a_{Hirth}	0.07 [37]	a_{Lomer}	0.122 [37]
a_{gliss}	0.137 [37]	a_{coll}	0.625 [37]
$\rho^s(T=0)$ (for all s)	$1\,\mu m^{-2}$	$\kappa^s_{screw}(T=0)$ (for all s)	$0\,\mu m^{-2}$
$\kappa^s_{edge}(T=0)$ (for all s)	$0\,\mu m^{-2}$	$q^s(T=0)$ (for all s)	$0\,\mu m^{-3}$
$L_x \times L_y \times L_z$	$18 \times 6 \times 18\,\mu m$		
Tribological loading parameters			
R_{indent}	20 µm	$\mathbf{C}_{indent}(T=0)$	(9, 26, 9) µm
$\mathcal{F}_{applied}$	1 mN	v_{slid}	15 mm/s
L_{stroke}	6 µm	$\mu_{friction}$	0.25 [6]
Numerical parameters			
N, M	120, 100	ξ_{force}	1×10^{-6} mN
ξ_y	1×10^{-6} GPa	ω_0	5.0 mN/µm
M_{indent}	26 500	ξ_{indent}	1×10^{-6} mN

3.1. Surface topographies induced by nano-indentation

In order to validate the proposed numerical model, we compare experimental observations for a nano-indentation test with the numerical results derived by the force-controlled numerical model for three high symmetric crystallographic planes: ND = (010), (110), and (111). In this test, $\mathcal{F}_{applied} = 20$ mN is applied with R_{indent} set to be 2 µm. The material dimensions are defined as $L_x \times L_y \times L_z = 18 \times 8 \times 18\,\mu m$ with an initial dislocation density $\rho^s = 1\,\mu m^{-2}$ across all 12 slip systems.

Simulated surface topographies under nano-indentation are shown in Figs. 7(a), 7(b), and 7(c), with the color scale indicating displacement along the loading (y-) direction (red: out-of-plane, blue: in-plane). The results capture the well-known anisotropic pile-up patterns consistent with crystallographic orientation – fourfold symmetry for ND = (010), twofold for ND = (110), and threefold for ND = (111) – in agreement with experimental observations [42–44]. The simulated profiles show good agreement with AFM measurements, e.g. by [43], as illustrated in Fig. 7(d) (ND = (001)), Fig. 7(e) (ND = (011)), and Fig. 7(f) (ND = (111)).

Due to the symmetry of the Thompson tetrahedron, the simulated surface profiles for ND = (010) and ND = (110) are expected to correspond to those for ND = (001) and ND = (011), respectively. Although the crystallographic orientation affects different slip systems activated under the indentation, the slip geometries are crystallographically equivalent, leading to similar deformation patterns. The visible in-plane rotation of 45° in the profiles for the simulation for ND = (010) and the experiment for ND = (001) is therefore expected for the considered orientations.

For ND = (111), the simulation result in Fig. 7(c) shows a threefold symmetry, whereas the experimental result in Fig. 7(f) exhibits a six-fold pattern. One possible explanation is the influence of indentation conditions. In our simulations, a six-fold symmetry also appears under increased indentation load. Since the experimental study does not specify the indenter size or load, a deviation in these quantities is considered likely. However, the same three-fold symmetry as in the present simulation has been also observed before in experimental results in [45], which applied an indenter of similar size (3.4 µm radius).

3.2. Dislocation trace line

We characterize the accumulation of GND densities at a specific depth beneath and parallel to the sliding surface in Fig. 8 under the setup 010_A.

The subsurface dislocation density distributions for different numbers of sliding stokes is depicted in Fig. 8. Figs. 8(b) and 8(d) show the cross after the first sliding stroke and Figs. 8(c) and 8(e) show the results after the ninth sliding stroke. It can be observed that the evolution yields the formation of DTLs over one and multiple sliding process. The data extraction path used here and the considered cross-section for the figures are illustrated in Fig. 8(a).

Fig. 8(b) displays the distribution of the sum of the screw dislocation density component of the GND density ($\Sigma|\kappa^s_{screw}|$ across the 12 slip systems), the edge dislocation density component of the GND density ($\Sigma|\kappa^s_{edge}|$ across the 12 slip systems), and the norm of the GND density vector ($\Sigma|\boldsymbol{\kappa}^s|$ across the 12 slip systems) after the first sliding stroke. Dislocation density is found to accumulate at a depth of approximately 0.312 µm beneath the deformed surface, primarily contributed by the edge components. This GND accumulation we identify as a first DTL.

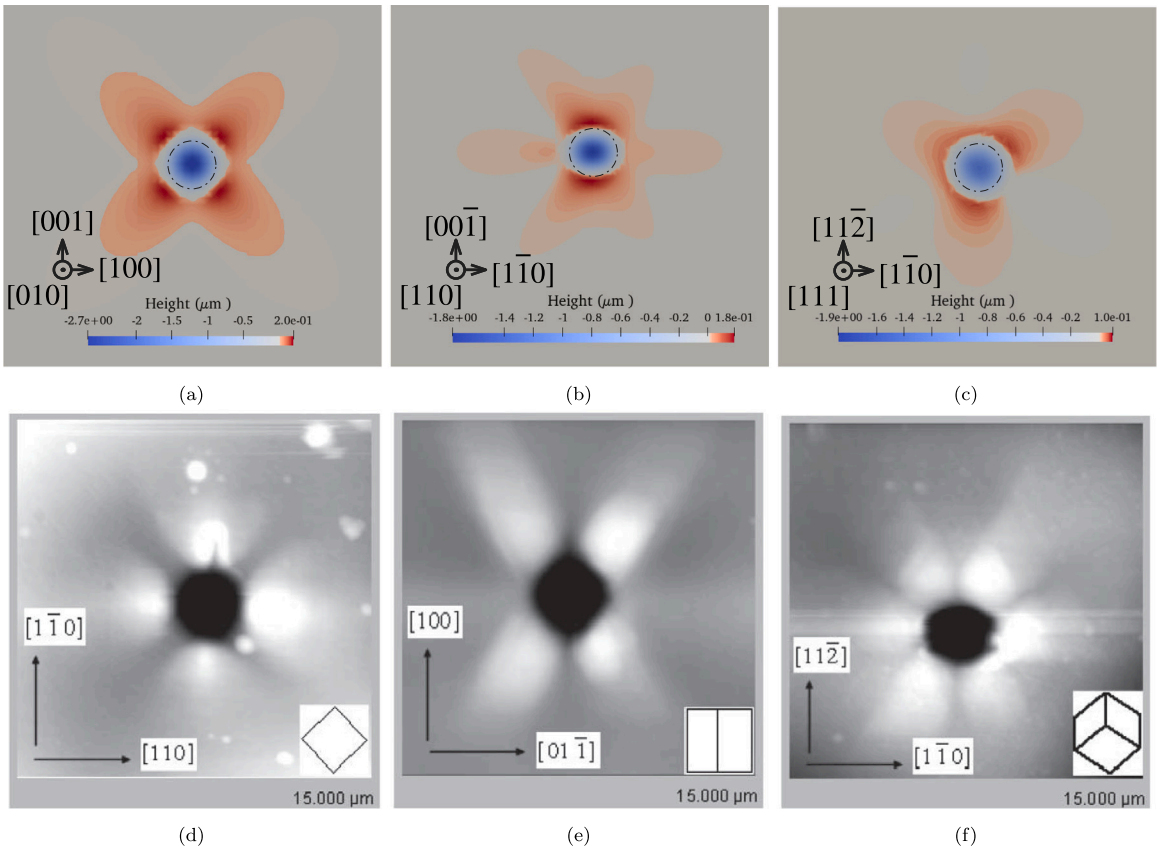

Fig. 7. Comparison of simulation and experimental results for nano-indentation test. Top-view of the indentation-induced surface topographies in comparison with experimentally observed data measured by [43]. (a), (b), and (c) are the simulation results while indenting on the planes with ND equals to (a) (010), (b) (110), and (c) (111). The black dash-dotted line circles indicate the size and position of the indenter. And (d), (e), and (f) are AFM image measured by [43] with ND equals to (a) (001), (b) (011), and (c) (111).

The cross-sectional view of the edge GNDs ($\Sigma|\kappa^{s}_{edge}|$) at the same time step is provided in Fig. 8(d), where the accumulation line beneath and parallel to the sliding surface at a certain depth is visible.

After the ninth sliding stroke, shown in Fig. 8(c), the boundary of the first DTL becomes less distinct and shifts deeper into the surface, now located at a depth of 0.403 μm. Additionally, a second dislocation accumulation is observed at a depth of 1.768 μm, which we identify as the second DTL. Both DTLs are primarily composed of edge components. The cross-sectional view of the edge GNDs at the same time step is shown in Fig. 8(e).

3.3. Misorientation after the first sliding stroke

Crystal rotation is a key phenomenon in crystalline materials under tribological loading. In this section, alongside the formation of dislocation trace lines discussed in Section 3.2, we present the misorientation distribution after the first sliding stroke, derived from the simulated $\boldsymbol{\kappa}$ field. The calculation procedure is detailed in Appendix B.

The magnitude for the lattice misorientation angle around the x-direction (SD), $|\varphi_x|$, is shown in Fig. 9(a); around the y-direction (ND), $|\varphi_y|$ in Fig. 9(b); and around the z-direction, $|\varphi_z|$ in Fig. 9(c). We can see the pronounced crystal rotation occurs at a depth of around 439 nm. The rotation around ND ($|\varphi_x|$) has the highest value of around 11°.

Since the misorientation is computed from the GND distribution, we also present the sum of the screw component GNDs ($\Sigma|\kappa^{s}_{screw}|$) in Fig. 9(d). The results indicate that rotation around the x- (SD) and z-directions is primarily driven by screw component GNDs, while rotation around the y-direction (ND) mainly arises from edge component GNDs, as shown in Fig. 8(d).

3.4. Dislocation transport under tribological loading

We display the results for the dislocation transport process driven by the stress field induced by tribological loading. Using the 010_A setup, we analyze the cross-section on the xz-plane (the ND-plane) at $y = 5.457$ μm, where the position of the first DTL after one sliding stroke has been found, as shown in Fig. 8(b).

Fig. 10 displays the evolution of dislocation density transport under tribological loading. We depict the screw (first column) and edge (second column) dislocation density components separately for clarity. The results show how dislocations are transported following the indenter's sliding motion (indicated by the white arrows). It can be observed that the edge component forms more stable dislocation accumulation directly beneath but a bit behind the indenter center (indicated by the yellow arrows) as well as in front of the contact area. In addition, the dislocation accumulation moves along with the sliding motion. Conversely, the screw dislocation density component tends to form an accumulation in front of the contact area rather than beneath the center, while also being transported with the indenter. Furthermore, both edge and screw components form dislocation accumulation along the sides of the sliding groove.

The results presented in Fig. 10 are depicted exemplarily for the 010_A setup. However, the computations have been done for all four setups as listed in Table 2. The different setups show qualitatively comparable dislocation density transport phenomenon and are for brevity not shown here for all setups in detail. Only the dominant dislocation density components beneath the indenter center, in front of the contact area, and along the groove sides change according to the crystal orientation.

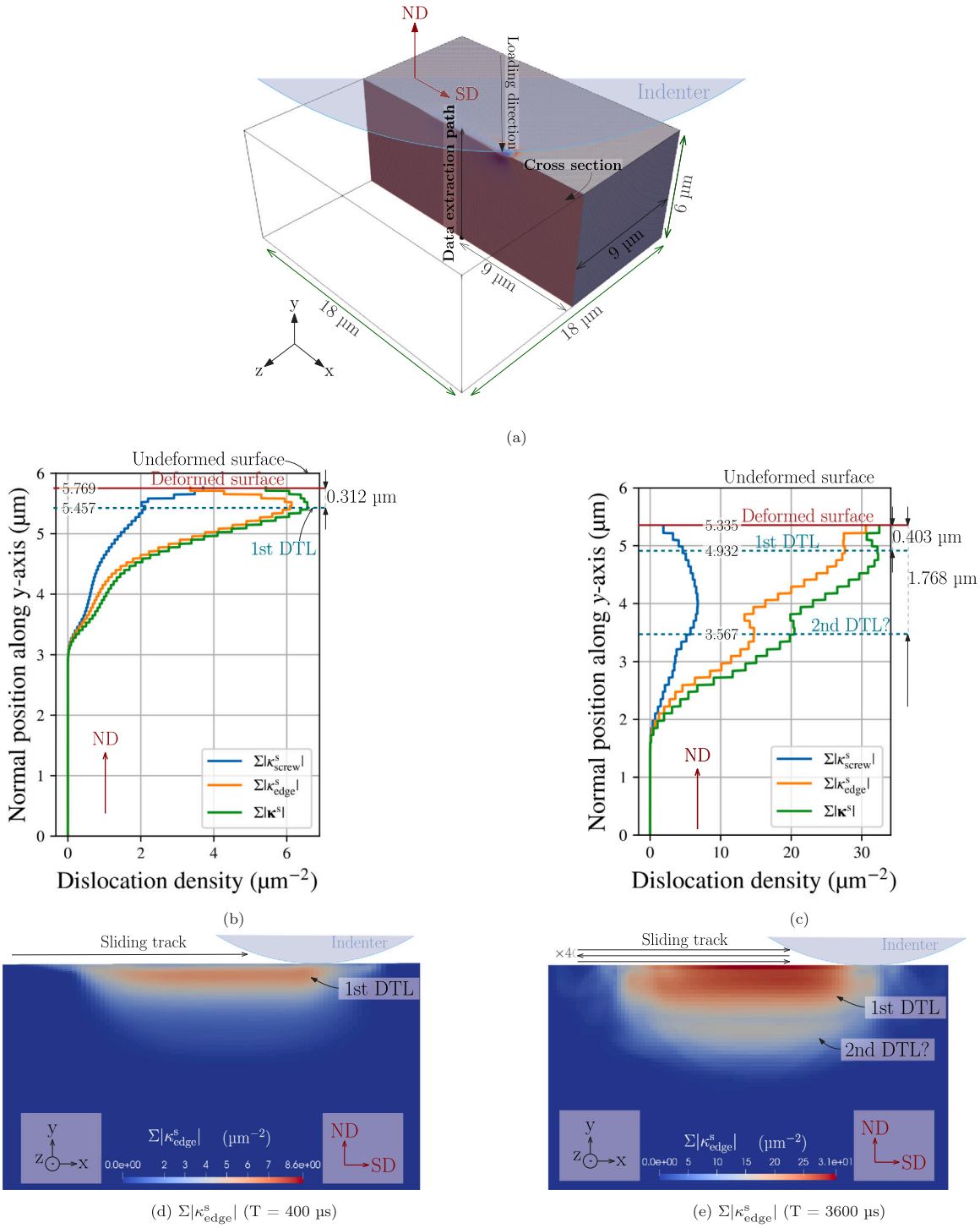

Fig. 8. Dislocation distribution along the *y*-axis (ND). (a) defines the data extraction path of dislocation densities for (b) and (c) and cross-section for (d) and (e). (b) and (c) demonstrate different types of dislocation density distributions along the *y*-axis at $T = 400\,\mu s$ and at $T = 3600\,\mu s$ respectively. (d) and (e) are the distribution of edge component GND densities at the cross-section of *xy*-plane at $z = 9$ μm when $T = 400\,\mu s$ and $T = 3600\,\mu s$ respectively.

3.5. Surface topographies induced by tribological loading under various crystal orientations

To evaluate the sensitivity of crystal orientation to plastic deformation under tribological loading, we analyze the surface topographies for the four crystallographic setups listed in Table 2. The topographies are evaluated after one forward sliding stroke as shown in Fig. 11. The data was extracted along the *z*-axis at the sliding groove's center ($x = 9\,\mu m$, $y = 6\,\mu m$), as illustrated in Fig. 11(a). Surface profiles for the setups with ND = (111) and (010) are presented in Figs. 11(b) and 11(d), respectively.

For ND = (111), Fig. 11(b) shows the surface topographies of setups 111_A and 111_B. In setup 111_A, the surface pile-up along the sliding groove is nearly symmetrical, whereas setup 111_B produces an

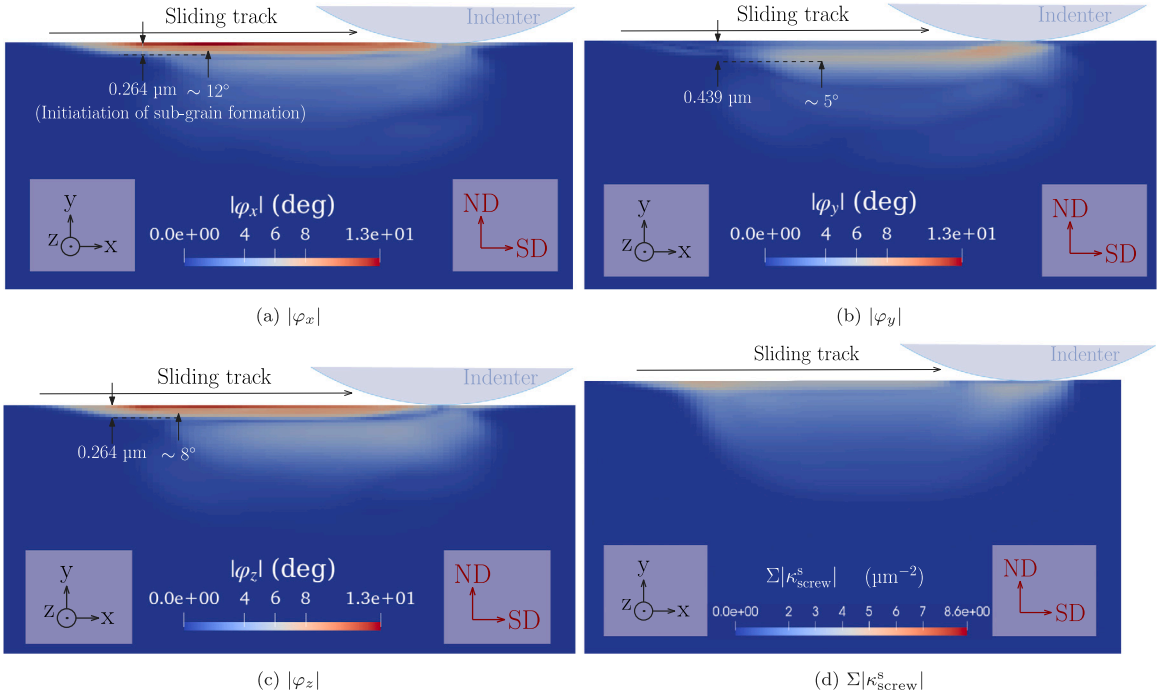

Fig. 9. The magnitude of misorientation around (a) x- (SD), (b)y- (ND), and (c)z-directions after the first sliding stroke at the cross-section of xy-plane at $z = 9$ μm when $T = 400$ μs. For comparison, (d) shows the distribution of the screw component GNDs, complementing the edge component distribution presented in Fig. 8(d).

asymmetrical surface topography, with material pile-up on the right-hand side (facing toward the SD direction) and sink-in on the left-hand side. Additionally, the distribution of total plastic slip, $\Sigma|\gamma^s|$ across all 12 slip systems, is shown for both setups. We find that setup 111_B exhibits an asymmetrical distribution of plastic slip as well. The side with higher values of plastic slip corresponds to the material pile-up, while the lower values of plastic slip correspond to the material sink-in. Furthermore, a higher overall magnitude of plastic slip and deeper groove can be observed compared to the setup 111_A.

Because plastic deformation results from dislocation motion with the velocity driven by resolved shear stress, in Fig. 11(c), we also show the distributions of the total resolved shear stress $\Sigma|\tau^s|$ and dislocation velocity $\Sigma|v^s|$ across all 12 slip systems for both setups. The results are taken while the indenter was at $x = 9$ μm and $z = 9$ μm. Fig. 11(c) shows that also the $\Sigma|\tau^s|$ and $\Sigma|v^s|$ distributions are influenced by the crystallographic characteristics. The distribution correlate with the plastic slip distribution $\Sigma|\gamma^s|$ shown in Fig. 11(b).

For ND = (010), the surface topographies for both setups, 010_A and 010_B, exhibit symmetrical features as shown in Fig. 11(d). To further explore the impact of frictional force on plastic deformation under different sliding directions, we also plot the surface topographies of these setups under two frictional conditions: $\mu_{friction} = 0$ (no friction) and $\mu_{friction} = 0.25$ (with friction) in Fig. 11(d). The result reveals that frictional force significantly influences the plastic deformation in setup 010_A, whereas its effect is less pronounced in setup 010_B.

3.6. Tribological contact area evolution considering plastic deformation

To assess the evolution of the tribological contact area influenced by plastic deformation, we demonstrate the changes in the contact area over multiple sliding strokes for the crystallographic setup 010_A, as depicted in Fig. 12. The color legend represents the total strain along the loading direction (y-axis), with the contact area shown as the dark-blue region, corresponding to the highest strain along the loading direction.

Considering the initial condition of a perfectly flat surface, Fig. 12(a) shows a nearly circular contact shape after the first half stroke. As sliding continues, Figs. 12(b), 12(c), and 12(d) display the evolution results of the contact area after 1.5, 3.5, and 8.5 strokes, respectively. It can be observed in Fig. 12(a), that there is a gradual transition of the contact area from a circular to an oval shape as the number of strokes increases.

4. Discussion

4.1. The physical interpretation of the numerical flux derived using the flux vector splitting method

In this section, we discuss the physical interpretation of the numerical flux formulation derived using the upwind scheme through the FVS method, as detailed in Section 2.2. The approach begins by decomposing the Jacobian matrix $\mathbf{J}(\mathbf{Q})$ along $\mathbf{l}^s$ and $\mathbf{d}^s$ into $\mathbf{J}_{\mathbf{l}^s}$ and $\mathbf{J}_{\mathbf{d}^s}$. We then solve the eigenvalue problem for $\mathbf{J}_{\mathbf{l}^s}$ and $\mathbf{J}_{\mathbf{d}^s}$ separately. A second splitting further divides $\mathbf{J}_{\mathbf{l}^s}$ and $\mathbf{J}_{\mathbf{d}^s}$ into positive and negative eigenvalue components. Thus, the approach splits the numerical flux on each face into four components, combining positive/negative and line/Burger's directions, as shown in Eq. (27). For a hexahedral cell with six faces, this method leads to a total of 24 terms for the flux computation, as detailed in Eq. (34). The terms represent either positive/negative contributions or are zero, depending on the flux direction. This implies that the splitting simplifies the identification of inner face flux directions, particularly in cases involving complex propagation directions.

The numerical flux derived in this study builds upon the framework for solving the eigenvalue problem, as detailed in [22,35]. By employing a flux splitting method to identify inner face flux directions, we achieve a stable numerical flux. A similar splitting concept has been introduced by [46]. However, instead of integrating the splitting process with solving the eigenvalue problem, [46] decomposes the dislocation density into positive/negative and edge/screw components.

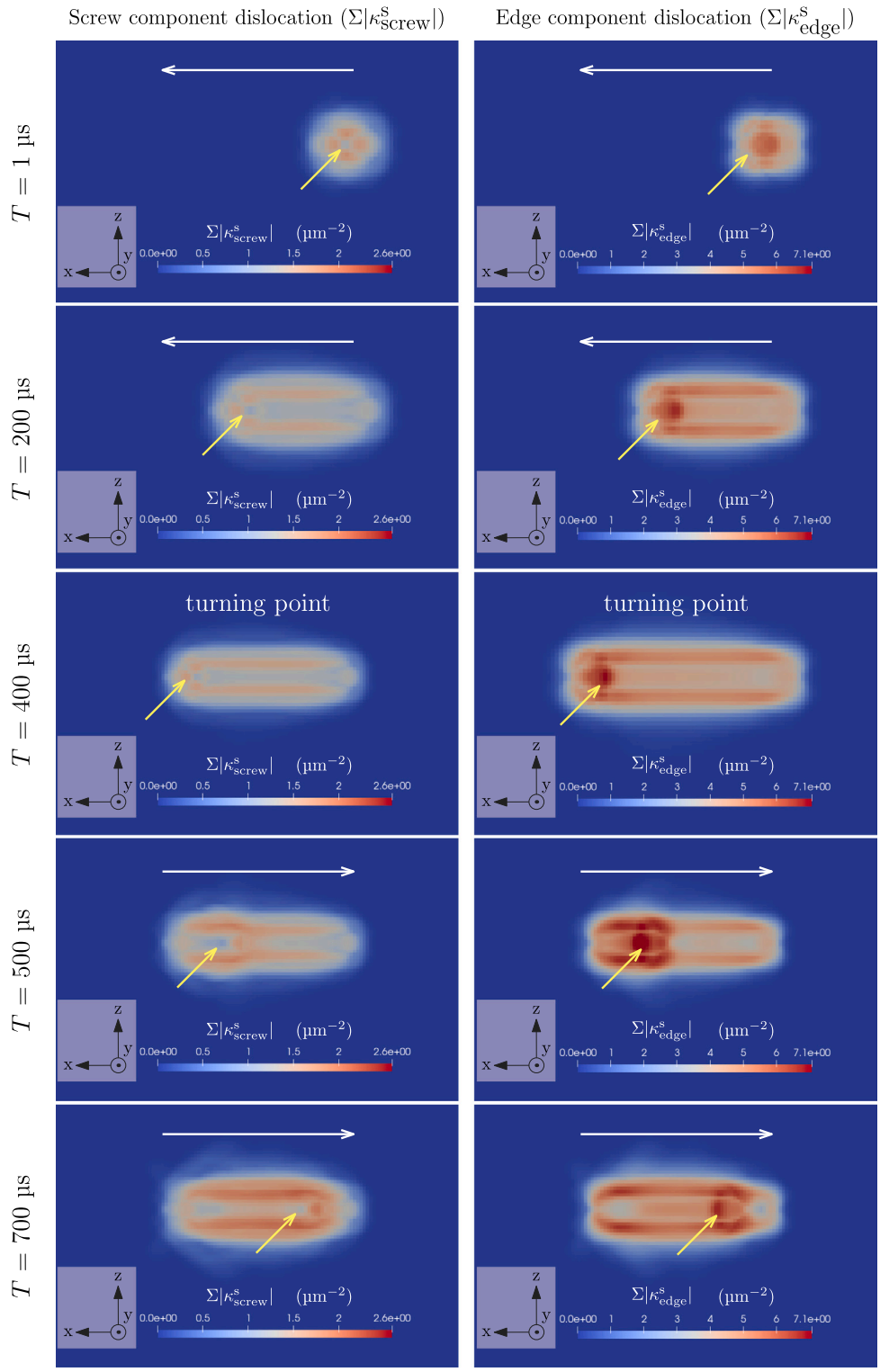

Fig. 10. The screw and edge components of the dislocation density transported by the tribological loading given exemplarily for the setup 010_{A}. The cross-section of observation is on the xz-plane at $y = 5.457\,\mu m$. The white arrow denotes the sliding direction of the indenter, while the yellow arrow indicates the indenter's center.

Therefore, the method is limited by not accounting for the curvature flux in the numerical flux derivation. It is remarked, that our approach presented, however, includes the same numerical flux as the method presented in [46] if the flux term for the curvature is neglected by omitting the third components of the Jacobian matrices, $\mathbf{J}_{|s}$ and $\mathbf{J}_{d^s}$.

The numerical stability of dislocation transport computation using the numerical scheme derived is examined through two benchmark cases: the edge dislocation dipole wall separation (Appendix A.3) and the dislocation loop expansion (Appendix A.4). From the two cases, we show the derived numerical scheme demonstrates positivity preserving

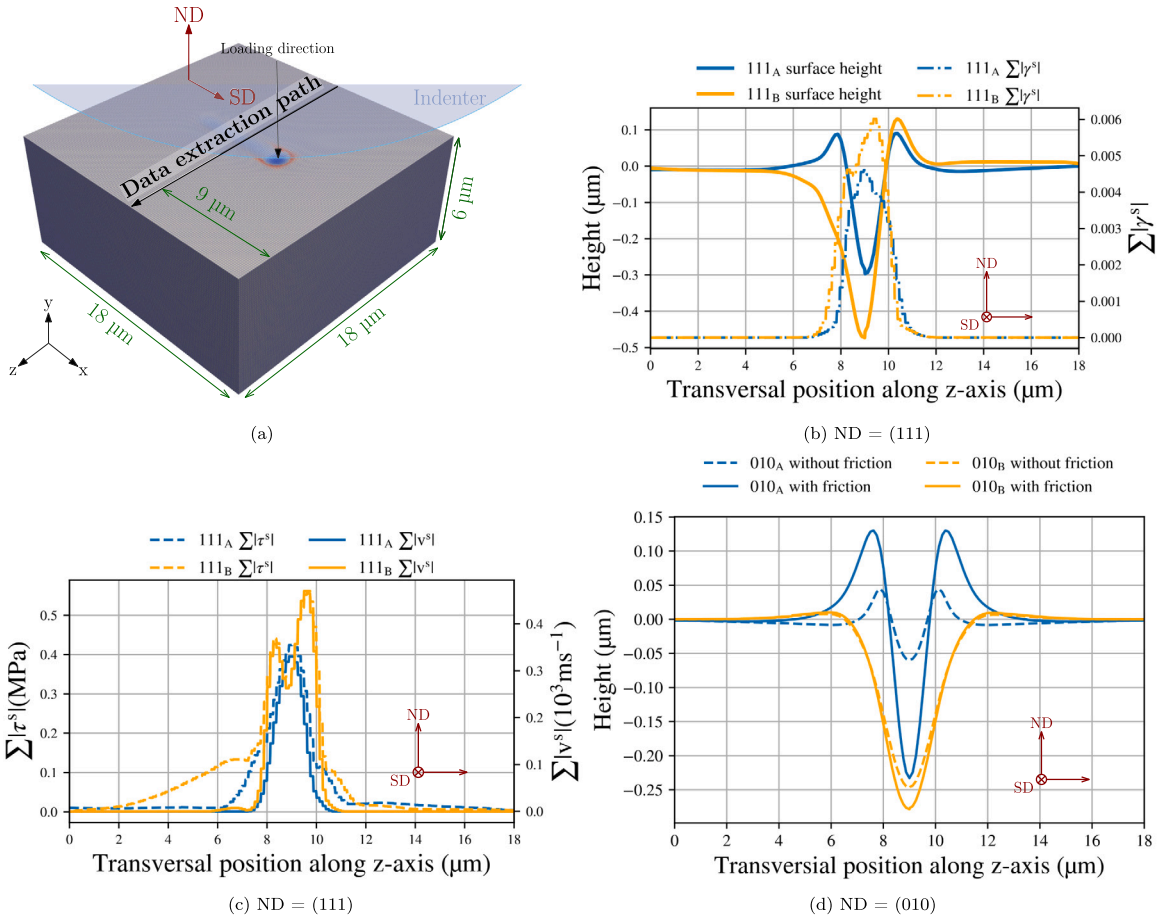

Fig. 11. Results after completing one sliding stroke under various crystallographic setups. (a) illustrates the data extraction path for all measurements. (b) presents the simulation results for surface topography and the sum of plastic slip across all 12 slip systems for ND = (111). (c) shows the sum of resolved shear stress and dislocation velocity for ND = (111) while the indenter is at the position of $x = 9\,\mu m$. (d) depicts the surface topography for ND = (010), comparing conditions with and without frictional force.

and numerical stability under both the condition with and without the effect of dislocation bow-out.

4.2. Dislocation trace line and crystal rotation in the subsurface area

Linear discontinuities, referred to as DTLs parallel to the surface, have been reported in experimental studies, see [5–7], for copper under tribological loading. These DTLs have been assumed to be dislocation lines with accumulated Burgers vector density, causing contrast variations and marking discrete crystal rotation changes. Our simulations show that this observation actually results from the excessive dislocation density ($\boldsymbol{\kappa}$) accumulation already visible after the first sliding stroke.

The presented model reveals that after one sliding stroke, GND densities accumulate beneath the surface, forming the first DTL mainly composed of edge components at a depth of $0.312\,\mu m$ for setup 010_A, as shown in Figs. 8(b) and 8(d). With an increased number of sliding strokes to 9, a second DTL appears at a depth of $1.768\,\mu m$, as shown in Figs. 8(c) and 8(e). Experimental studies have also been reported the first DTL at depths of several hundred nanometers, consistent with the GND accumulation in this study. However, the second DTL in the simulation appears at a greater depth than typical experimental observations are able to reveal, which usually report depths of less than $1\,\mu m$. The deviation in predicting the position of the second DTL may stem from the absence of dynamic crystal rotation coupling with the loading process in the current model. As misorientation develops after the first cycle (shown in Fig. 9), the resulting crystallographic mismatch could affect subsequent dislocation behavior, especially as the sliding stroke increase. Experimental studies have also found that the first DTL appear after merely one sliding stoke, and with increasing number of passes of stokes, a second DTL at a deeper position is visible [6]. It is also in consistent with the results we observed with our simulation model.

The presence of GND densities is consistent with lattice rotation, as described by [47]. Fig. 9 shows the misorientation distribution after the first sliding stroke, compared to the undeformed state. These results demonstrate that the proposed model captures the onset of crystal rotation, which marks the initiation of sub-grain formation under tribological loading. Experimental studies have shown that, over time, such rotations evolve into small-angle grain boundaries forming sub-grains in the subsurface region. However, in this work, crystal rotation is evaluated only through post-processing of the $\boldsymbol{\kappa}$ distribution so far. To improve accuracy of the model for crystal rotation and sub-grain evolution under repeated sliding, future model development should incorporate the dynamic coupling along the loading process and continuous lattice rotation.

Currently, no existing simulation model, whether discrete or continuum, can fully capture the formation of DTLs and sub-grains under tribological loading. This study demonstrates the potential of the proposed dislocation-based crystal plasticity model to simulate the formation of these important microstructure features observed in tribology experiments. Future work may support experimental studies to better understand the formation of these features.

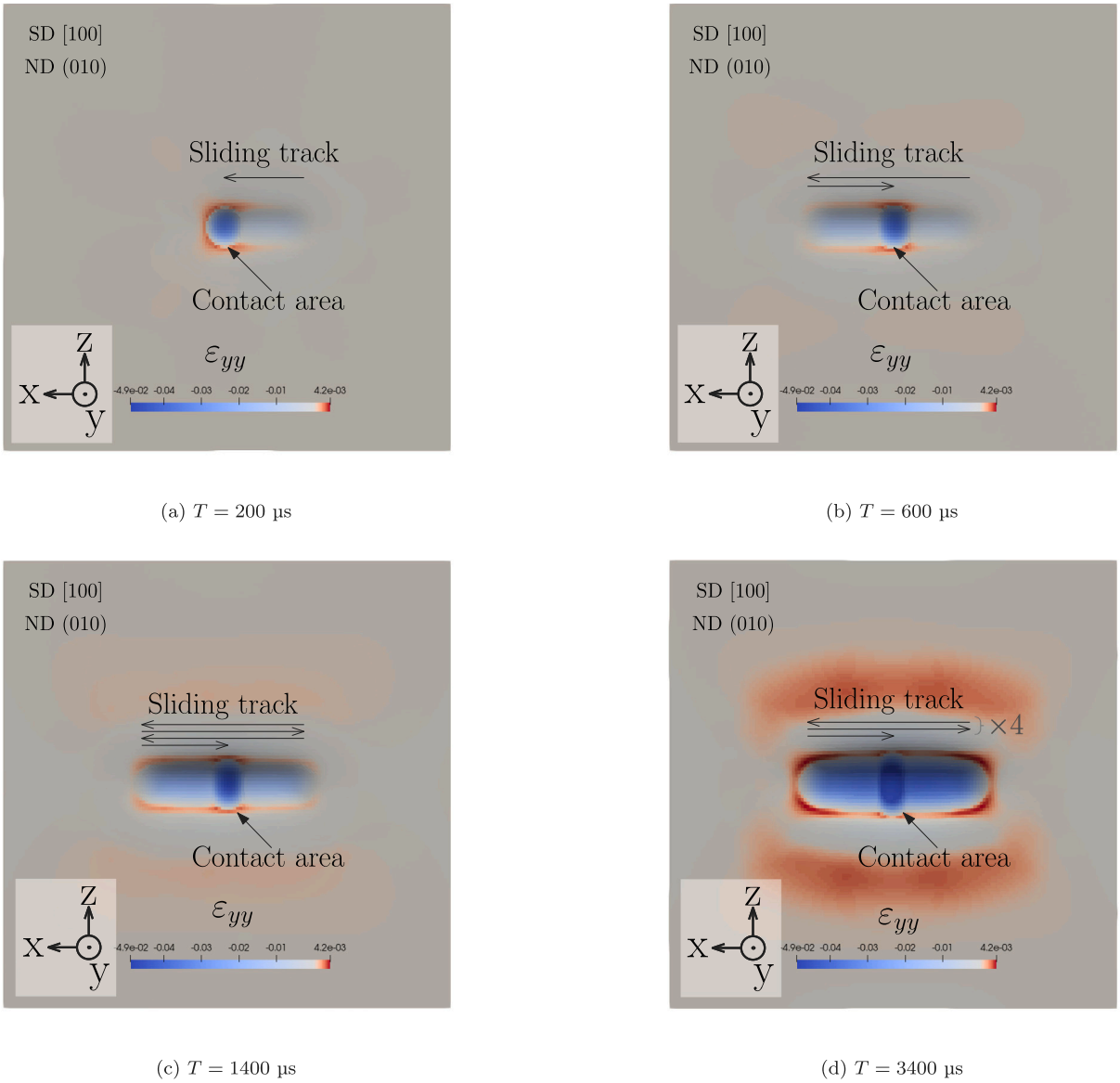

(a) $T = 200$ µs (b) $T = 600$ µs

(c) $T = 1400$ µs (d) $T = 3400$ µs

Fig. 12. Evolution of the contact area under tribological loading over multiple strokes.

4.3. Dislocation transport and plastic deformation under tribological loading

In Section 3.4, we illustrate the dislocation transport phenomenon driven by tribological loading, as simulated using the dislocation-based crystal plasticity model developed in this study. Similar phenomena have been observed in DDD simulations due to the stress field induced by an indenter's sliding [2]. Notably, [2] also highlight that classical continuum mechanics or standard crystal plasticity methods cannot effectively consider the effect of dislocation transport and cannot account for plastic deformation associated with it. However, this phenomenon, characterized by large-scale dislocation glide, is critical as dislocation glide is a primary mechanism driving plastic deformation.

The plastic deformation caused by dislocation dynamics appears as material pile-up and sink-in along the sliding groove. [3] highlights that these behaviors depend heavily on crystal orientation. Standard crystal plasticity methods, however, are usually not sensitive to crystallographic effects under tribological loading. They are often not able to accurately predict dislocation pile-ups while discrete simulations are not able to capture that large length scales. In Fig. 11(c), we show that the dislocation velocity, driven by resolved shear stress, is strongly influenced by the crystal orientation. This observation affects plastic deformation and leads to the distinct symmetrical and asymmetrical surface topographies observed in setups 111_A and 111_B in Fig. 11(b).

The symmetric and asymmetric plastic deformation can be interpreted using the Thompson tetrahedron, as illustrated in Figs. 6(a) and 6(b) for 111_A and 111_B, respectively. Facing the positive SD direction, the 111_B setup shows distinct slip system activity on both sides of the sliding groove: slip systems parallel to the surface (2 and 4) dominate on the left-hand side, while those nearly perpendicular to the surface (1 and 3) dominate on the right. Consequently, the crystallographic configuration of 111_B results in deeper resolved shear stress influence perpendicular to the surface on the right and a broader spread of stress parallel to the surface on the left. This distribution leads to a similar pattern of dislocation velocity and plastic slip, and therefore plastic deformation on the surface under sliding. In contrast, the 111_A

setup shows symmetrical dislocation mobility on both sides of the groove, producing a nearly symmetrical pattern in surface topography. Observing the Thompson tetrahedron for 010_A and 010_B in Figs. 6(c) and 6(d), these setups also exhibit symmetrical dislocation mobility and result in symmetrical surface topography (Fig. 11(d)).

4.4. Influence of frictional force

In Fig. 11(d), the influence of a frictional force on the plastic deformation of the surface topographies is observed for the two setups with ND = (010) and different SD directions. As highlighted in [2], the frictional force increases the stress state and shifts the zone of maximum stress closer to the surface. Consequently, the stress distribution is altered due to frictional force. The result presented in Fig. 11(d) shows that the sensitivity of plastic deformation to frictional force is highly dependent on crystal orientation. This sensitivity indicates that further investigations of the role of the friction coefficient in dislocation transport and a systematic comparison for different crystal orientations should be conducted for a deeper understanding.

4.5. Tribological contact area evolution considering plastic deformation

In Section 3.6, we illustrate the evolution of the contact area over multiple sliding strokes under the symmetrical setup 010_A. The transition from Figs. 12(a) to 12(b) shows a substantial transformation in the contact area shape, changing from circular to oval even after a single stroke under the conditions of this study. This transformation is driven by surface plastic deformation caused by dislocation motion during sliding, as captured by the simulation model (Fig. 10 in Section 3.4). After the first stroke, the deformable material's surface topography is no longer flat (Section 3.5, blue solid curve in Fig. 11(d)). Instead, surface pile-ups form along the sliding groove's sides due to plastic deformation, causing the indenter tip to contact the groove's sides before its center, resulting in an elongated, oval-shaped contact area transverse to the groove.

Tribological contact characteristics are predominantly governed by plastic deformation [1–4]. This study highlights limitations in many approaches simplifying tribological contact using superposed analytical solutions, such as the Green's function method [18]. These models often assume purely elastic deformation and idealized geometries. For instance, Hamilton's solution [19] predicts stress fields for a spherical surface sliding against a semi-infinite plane, resulting in a circular contact area. However, such models neglect plastic deformation and surface geometry changes, leading to inaccuracies in stress fields once plastic deformation occurs. Moreover, elastic models often underestimate the true contact area and overestimate contact pressure under small loads [4]. Experimental studies also struggle to measure true contact area and pressure in non-transparent materials, leaving data gaps. The proposed methodology addresses these limitations, providing a realistic model for macro- and micro-scale material behavior under tribological contact mechanics.

5. Conclusion

We present a computational simulation framework based on dislocation-based crystal plasticity theory (CDD) to analyze macro- and micro-scale material behavior under tribological contact mechanics. To ensure numerical stability, we derived a numerical scheme using the flux vector splitting method to solve the CDD problem. An implicit coupling mechanism enables large simulation time steps and accurately captures dislocation evolution's influence on plasticity. To model material response under contact conditions, a penalty contact method with a Neumann boundary condition was introduced.

Using this model, we investigated material behavior under tribological contact, leading to the following conclusions:

- The proposed framework highlights and explains the formation of DTLs and their evolution beneath the surface, aligning with experimental observations of the position for the first DTL. This demonstrates its potential as a continuum crystal plasticity model for simulating microstructure feature in the subsurface region under tribological contact.
- The misorientation distribution after the first sliding stroke demonstrates the model's ability to predict the onset of sub-grain formation. However, dynamic coupling with lattice rotation during loading is needed for improved predictions under repeated cycles.
- The continuum model allows for explicit simulation of dislocation transport phenomena, a key mechanism for understanding plastic deformation under tribological loading. This has been realized on that length scale for the first time by the continuum model, in contrast to previous studies that were restricted to smaller scales applying DDD and MD simulations. By accounting for the effects of crystal orientation on resolved shear stress, dislocation velocity, and plastic slip, the model predicts both symmetrical and asymmetrical dislocation mobility and plastic deformation. This framework provides a methodology for analyzing material behaviors under tribological contact, including dislocation features and material pile-up and sink-in along sliding grooves under different crystal orientations, bridging the gap between continuum and discrete approaches.
- The sensitivity of plastic deformation to frictional force varies significantly with crystal orientation.
- The simulation methodology overcomes the limitations of adapting traditional elastic and idealized analytical solutions by accurately capturing the evolution of contact area and stress states influenced by plastic deformation at each time step, providing a more realistic and reliable approach for analyzing tribological contact mechanics, especially in a larger deformation regime.

Although the present study is purely numerical, the proposed simulation method provides a valuable foundation for connecting mesoscale simulations with experimental observations. It enables detailed investigation of subsurface processes in crystalline materials under tribological loading and offers a pathway for future validation. The method can assist in interpreting experimental findings related to microstructural features such as dislocation trace lines, sub-grain structures, and dislocation evolution under repeated loading. It also supports the analysis of macroscopic characteristics like surface topography, as well as the influence of different loading scenarios—such as the effect of frictional forces under varying crystallographic conditions. By bridging numerical simulations and experimental studies, the approach holds strong potential for advancing the understanding of complex material behavior under tribological loading.

CRediT authorship contribution statement

Sing-Huei Lee: Writing – original draft, Software, Methodology, Data curation, Investigation . **Christian Wieners:** Writing – review & editing, Methodology, Supervision . **Katrin Schulz:** Writing – review & editing, Methodology, Investigation, Supervision, Funding acquisition, Conceptualization.

Declaration of competing interest

The authors declare that they have no known competing financial interests or personal relationships that could have appeared to influence the work reported in this paper.

Acknowledgments

We gratefully acknowledge the financial support of this work in the context of the German Research Foundation (DFG) project SCHU 3074/3-1 and the funding by the Carl-Zeiss-Stiftung. The simulations were performed on the HoreKa supercomputer funded by the Ministry of Science, Research and the Arts Baden-Württemberg and by the Federal Ministry of Education and Research as well as on the HAICORE supercomputer supported by the Helmholtz Association Initiative and Networking Fund on the HAICORE@KIT partition. Furthermore, we also acknowledge the contributions and discussion with Dr. Niklas Baumgarten regarding the simulation software and Dr. Antje Dollmann and Malte Flachmann regarding experimental tribological contact problems.

Appendix A. Numerical benchmark tests and properties

We present several benchmark test cases to verify both the physical fidelity and stability of the numerical simulation with these tests. The material parameters are the same as the ones detailed in Section 2.6.

A.1. Convergence test of the mechanical response under indentation loading

We demonstrate the convergence behavior of the numerical scheme by simulating a displacement-controlled indentation problem, focusing on testing the numerical stability of the scheme derived for the micro-problem. To simplify the computational procedure, the boundary condition described in Section 2.4 is modified to a Dirichlet boundary condition. Specifically, the indenter is controlled by displacement, with its movement linearly related to the macro time T, such that $\mathbf{C}_{\text{indent}} = [0, -0.005T, 0]$ µm. As illustrated in Fig. 4, once penetration is detected (as shown in Fig. 4(b)), we impose the gap function as the Dirichlet boundary condition instead of calculating the force balance. Therefore, the Dirichlet boundary condition in Eq. (3a) becomes

$$\boldsymbol{u}_{\text{D}} = -\mathcal{G}(\mathbf{x}). \tag{A.1}$$

The indenter is loaded for 50 ns, reaching an indentation depth of 0.25 µm. The indenter is then held at this depth for 30 ns to allow for relaxation.

We test the displacement-controlled indentation problem at various spatial discretization levels. The macro problem uses Lagrange discretization with polynomial degree one, while the micro problem employs discontinuous Galerkin discretization with polynomial degree one. The five discretization levels, with corresponding element sizes and element counts, are listed in Table A.4.

Table A.4
Overview of discretization levels with corresponding element sizes and number of elements.

Level	0	1	2	3	4
Element size (µm)	1	0.5	0.25	0.125	0.0625
Number of elements	1 000	8 000	64 000	512 000	4 096 000

Table A.5
Convergence test for the contact boundary condition.

Level	0	1	2	3	4
Indented depth (nm)	0.2486	0.2974	0.1811	0.1577	0.1498
Responding force (mN)	0.05789	0.05793	0.05767	0.05732	0.05732
Maximum of τ^{s} (MPa)	4.2944	10.8495	11.1483	11.0401	11.4261

In Fig. A.13, the load–displacement curves demonstrate convergence behavior as the number of elements increases. When the discretization level exceeds level 2, the load–displacement curves show minimal differences, indicating sufficient convergence on the mechanical response influenced by the microstructure.

A.2. Convergence test for the contact boundary condition

We also performed a convergence test to evaluate the force balance between the applied force $\mathcal{F}_{\text{applied}}$ and the responding force from the deformed material under different discretization levels for the contact boundary condition.

The test use the force-controlled indentation problem, where a force of 0.05714 mN is applied with an indenter radius R_{indent} of set to be 0.5 µm. The material dimensions are defined as $\text{L}_x \times \text{L}_y \times \text{L}_z = 18 \times 8 \times 18$ µm with an initial dislocation density $\rho^{\text{s}} = 2\,\mu\text{m}^{-2}$ across all 12 slip systems.

The tests under different discretization levels detailed in Table A.4 are summarized in Table A.5. These responses include the indented depth (the deepest point of the indented material), the responding force (calculated by integrating σ_{yy} over the indented area on the deformed material), and the maximum value of τ^{s} throughout the material. The results show that, although the force balance between $\mathcal{F}_{\text{applied}}$ and the responding force is achieved at discretization level 0, all other mechanical responses converge when the discretization level exceeds level 3.

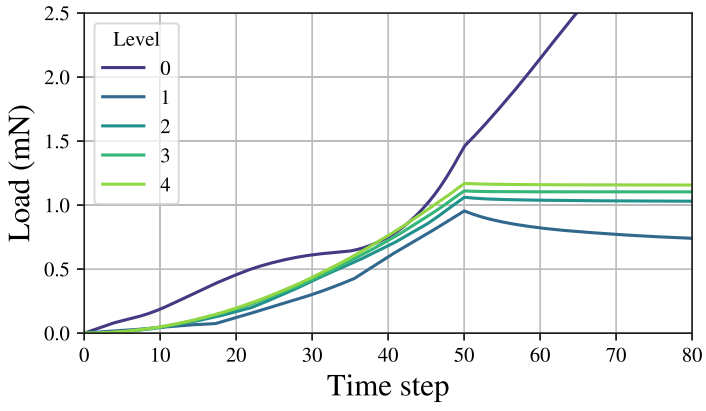

Fig. A.13. Convergence behavior in the load–displacement curves of solving indentation problem.

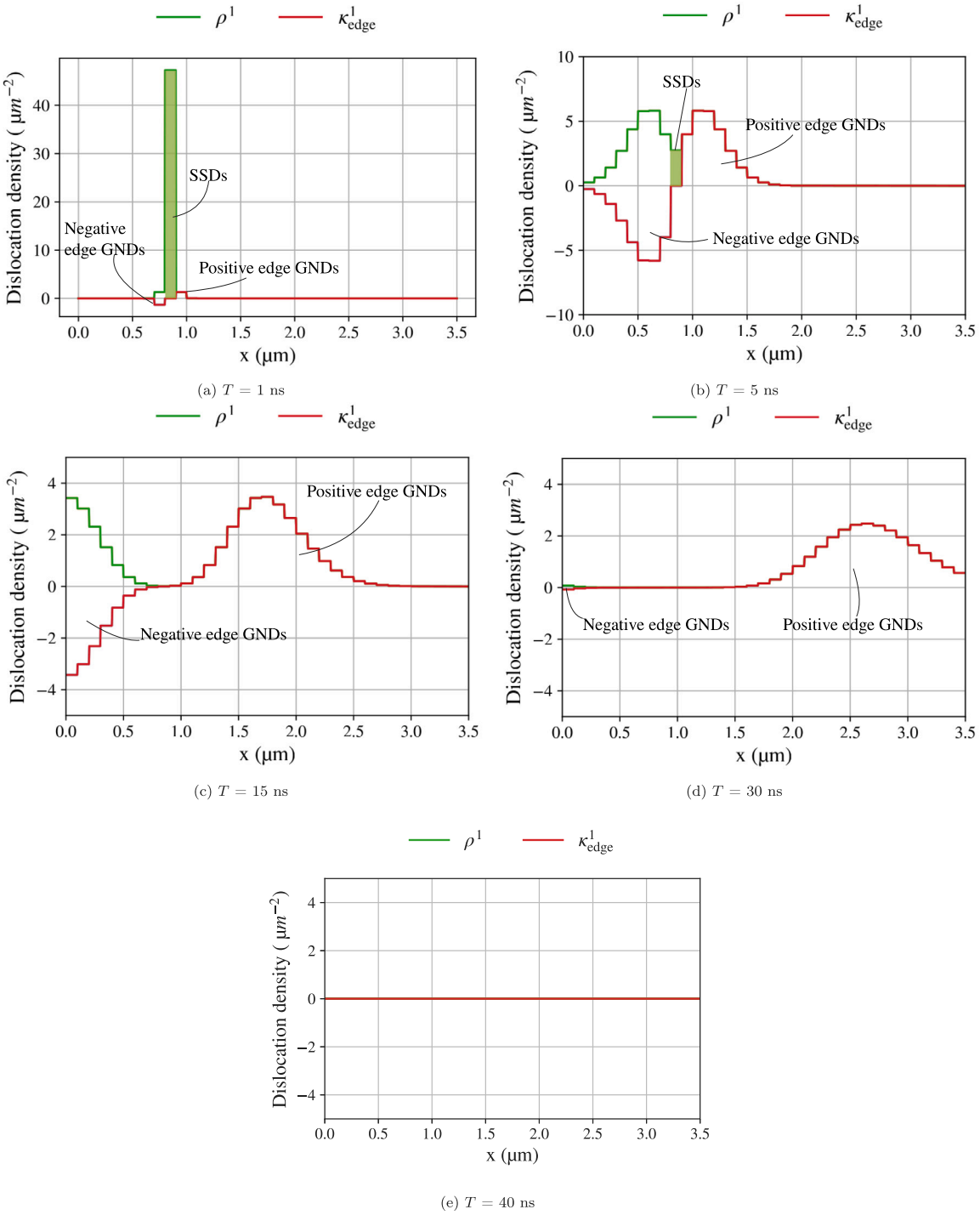

Fig. A.14. Benchmark result simulating the movement of a straight edge dislocation dipole wall.

A.3. Edge dislocation dipole wall separation

We also simulate the movement of a straight edge dislocation dipole wall. The system dimensions are $3.5 \times 0.1 \times 5\,\mu\text{m}$ in the x-, y-, and z-directions, with only one layer of elements. Each element is a $0.1 \times 0.1 \times 0.1\,\mu\text{m}$ hexahedron, using Lagrange discretization with polynomial degree equal to one and discontinuous Galerkin discretization with polynomial degree equal to zero (finite volume). We consider one slip system, with slip direction $\mathbf{d}^1 = (1, 0, 0)$ and line direction $\mathbf{l}^1 = (0, 1, 0)$. We place edge dipole walls by assuming the initial condition for the micro problem with an initial total dislocation density of $\rho^1 = 50\,\mu\text{m}^{-2}$ at positions ranging from $x = 0.8$ to $0.9\,\mu\text{m}$. For the macro problem, we assume a homogeneous external stress $\tau^s_{\text{ext}} = 200$ MPa throughout the system, as described in Eq. (10).

Since the dislocation walls are subjected to homogeneous τ^s_{ext}, they remain straight without bowing out. This test verifies dislocation transport across elements via the numerical flux detailed in Section 2.2 under simple conditions without dislocation bow-out. The results are shown in Fig. A.14, where the orange curve represents ρ^1, and the blue curve represents κ^1_{edge}. At $T = 1$ ns, most initial ρ^1 remain SSDs. Over time, SSDs convert into positive/negative edge GNDs and move into neighboring elements. During transport, i.e., at $T = 5$, 15, 30 ns, ρ^1 matches κ^1_{edge} without numerical error. This test demonstrates the

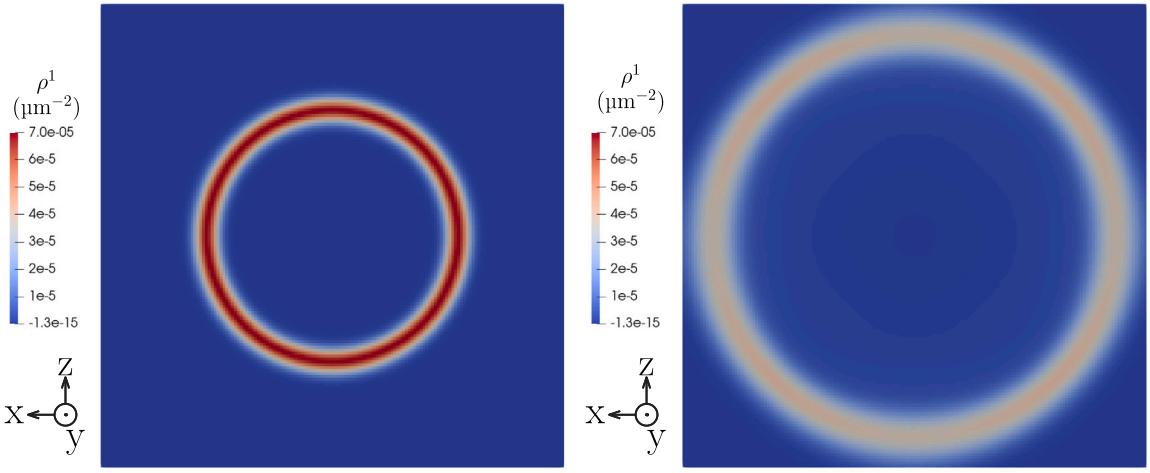

(a) ρ^1 at $T = 1$ ns

(b) ρ^1 at $T = 30$ ns

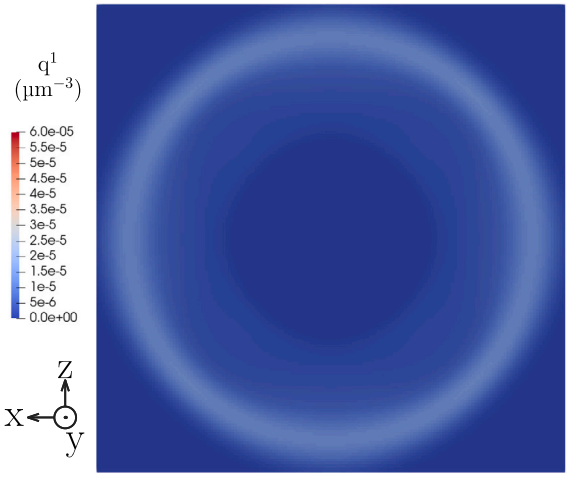

(c) q^1 at $T = 30$ ns

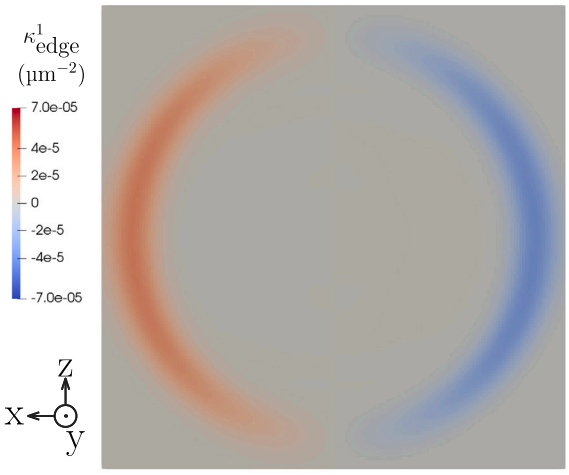

(d) κ^1_{edge} at $T = 30$ ns

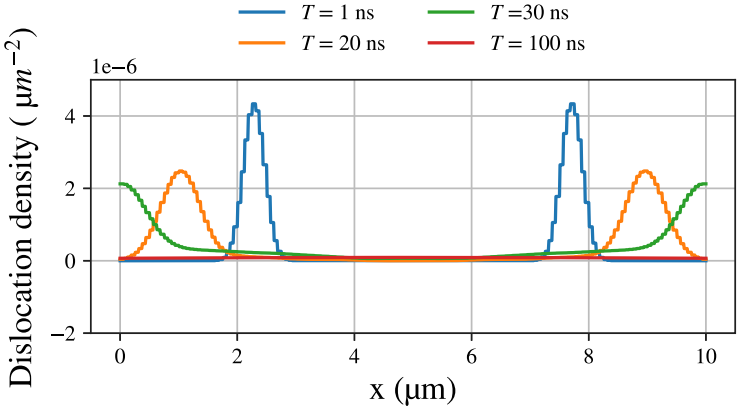

(e) Distribution of ρ^1 over time

Fig. A.15. Benchmark result simulating the expansion of a dislocation loop.

positivity-preserving nature of the derived numerical scheme without dislocation bow-out.

A.4. Dislocation loop expansion

We also simulate the expansion of a dislocation loop on a single slip system with slip direction $\mathbf{d}^1 = (1, 0, 0)$ and line direction $\mathbf{l}^1 = (0, 1, 0)$. The loop has an initial radius of 2.5 μm, following the setup in [35]. The system dimensions are $10 \times 0.2 \times 10$ μm along the x-, y-, and z-directions. Each element is a $0.0625 \times 0.0625 \times 0.0625$ μm hexahedron, with both Lagrange and discontinuous Galerkin discretization with polynomial degree equal to one applied.

The results in Figs. A.15(a) to A.15(d) show the evolution of ρ^1, q^1, and κ^1_{edge}, with κ^1_{screw} following a similar trend. These results

confirm that the proposed numerical scheme effectively converts the curvature density q^1 into the total dislocation density ρ^1 during loop expansion. The curvature density, introduced as a source term, compensates for missing dislocation density as the loop expands without causing divergence. This is demonstrated in the evolution of ρ^1 over time (Fig. A.15(e)). Introducing the curvature term enhances positivity preservation when dislocation bowing-out.

Appendix B. Calculation for misorientation from GND density

To facilitate comparison with experimental measurements such as electron backscatter diffraction (EBSD) or transmission Kikuchi diffraction (TKD), we derive the misorientation field from the simulated GND density distribution $\boldsymbol{\kappa}$.

Nye [47] characterize the lattice orientation change $\mathrm{d}\varphi_i$ with the lattice curvature tensor $\mathcal{K}_{ij}$ and the descritization length scale $\mathrm{d}x_j$ (dimension of the elements) along j

$$\mathrm{d}\varphi_i = \mathcal{K}_{ij}\mathrm{d}x_j. \tag{B.1}$$

And $\mathcal{K}_{ij}$ has the relation with dislocation tensor (Nye's tensor) α_{ij} as

$$\mathcal{K}_{ij} = \alpha_{ji} - \frac{1}{2}\delta_{ij}\alpha_{kk}. \tag{B.2}$$

From the simulation results proposed in this work, we calculate the dislocation density with excessive Burgers vector as the GND density $\boldsymbol{\kappa}^s$ for all slip systems from the CDD model. We can therefore estimate α_{ij} in terms of pure dislocations with screw and edge components based on the derivation detailed in Section 4 of [48]

$$\alpha_{ji} = \Sigma_{s=1}^{12}\left(\kappa^s_{\mathrm{screw}}\mathbf{d}^s \otimes \mathbf{d}^s + \kappa^s_{\mathrm{edge}}\mathbf{l}^s \otimes \mathbf{d}^s\right). \tag{B.3}$$

If we bring Eq. (B.3) back to Eq. (B.2), then to Eq. (B.1), we can estimate the misorientation φ around x-(SD), y-(ND), and z-directions.

Data availability

Simulation data and videos for all results will be available on request. The source code for the dislocation-based crystal plasticity simulation software realized in M++ is stored as a subproject under https://gitlab.kit.edu/kit/mpp. Access rights may also be granted upon reasonable request.

References

[1] Bhushan B. Nanotribology and nanomechanics: an introduction. Springer; 2008.
[2] Gagel J, Weygand D, Gumbsch P. Discrete dislocation dynamics simulations of dislocation transport during sliding. Acta Mater 2018;156:215–27.
[3] Irani N, Nicola L. Modelling surface roughening during plastic deformation of metal crystals under contact shear loading. Mech Mater 2019;132:66–76.
[4] Civiero R, Perez-Rafols F, Nicola L. Modeling contact deformation of bare and coated rough metal bodies. Mech Mater 2023;179:104583.
[5] Greiner C, Liu Z, Strassberger L, Gumbsch P. Sequence of stages in the microstructure evolution in copper under mild reciprocating tribological loading. ACS Appl Mater Interfaces 2016;8(24):15809–19.
[6] Greiner C, Liu Z, Schneider R, Pastewka L, Gumbsch P. The origin of surface microstructure evolution in sliding friction. Scr Mater 2018;153:63–7.
[7] Haug C, Ruebeling F, Kashiwar A, Gumbsch P, Kübel C, Greiner C. Early deformation mechanisms in the shear affected region underneath a copper sliding contact. Nat Commun 2020;11(1):839.
[8] Zaafarani N, Raabe D, Roters F, Zaefferer S. On the origin of deformation-induced rotation patterns below nanoindents. Acta Mater 2008;56(1):31–42.
[9] Engels P, Ma A, Hartmaier A. Continuum simulation of the evolution of dislocation densities during nanoindentation. Int J Plast 2012;38:159–69.
[10] Reuber C, Eisenlohr P, Roters F, Raabe D. Dislocation density distribution around an indent in single-crystalline nickel: Comparing nonlocal crystal plasticity finite-element predictions with experiments. Acta Mater 2014;71:333–48.
[11] Wang Z, Zhang H, Li Z, Li G, Zhang J, Zhang J, ul Hassan H, Yan Y, Hartmaier A, Sun T. Crystal plasticity finite element simulation and experiment investigation of nanoscratching of single crystalline copper. Wear 2019;430:100–7.
[12] Gagel J, Weygand D, Gumbsch P. Formation of extended prismatic dislocation structures under indentation. Acta Mater 2016;111:399–406.
[13] Zhu T, Li J, Van Vliet KJ, Ogata S, Yip S, Suresh S. Predictive modeling of nanoindentation-induced homogeneous dislocation nucleation in copper. J Mech Phys Solids 2004;52(3):691–724.
[14] Begau C, Hartmaier A, George EP, Pharr GM. Atomistic processes of dislocation generation and plastic deformation during nanoindentation. Acta Mater 2011;59(3):934–42.
[15] Gao Y, Ruestes CJ, Tramontina DR, Urbassek HM. Comparative simulation study of the structure of the plastic zone produced by nanoindentation. J Mech Phys Solids 2015;75:58–75.
[16] Voyiadjis GZ, Yaghoobi M. Review of nanoindentation size effect: Experiments and atomistic simulation. Crystals 2017;7(10):321.
[17] Zhou N, Elkhodary KI, Huang X, Tang S, Li Y. Dislocation structure and dynamics govern pop-in modes of nanoindentation on single-crystal metals. Phil Mag 2020;100(12):1585–606.
[18] Vakis AI, Yastrebov VA, Scheibert J, Nicola L, Dini D, Minfray C, Almqvist A, Paggi M, Lee S, Limbert G, et al. Modeling and simulation in tribology across scales: An overview. Tribol Int 2018;125:169–99.
[19] Hamilton GM. Explicit equations for the stresses beneath a sliding spherical contact. Proc Inst Mech Eng Part C: J Mech Eng Sci 1983;197(1):53–9.
[20] Baumgarten N, Wieners C. The parallel finite element system M++ with integrated multilevel preconditioning and multilevel Monte Carlo methods. Comput Math Appl 2021;81:391–406. http://dx.doi.org/10.1016/j.camwa.2020.03.004.
[21] Hochrainer T. Multipole expansion of continuum dislocations dynamics in terms of alignment tensors. Phil Mag 2015;95(12):1321–67.
[22] Schulz K, Wagner L, Wieners C. A mesoscale continuum approach of dislocation dynamics and the approximation by a Runge-Kutta discontinuous Galerkin method. Int J Plast 2019;120:248–61.
[23] Hochrainer T, Sandfeld S, Zaiser M, Gumbsch P. Continuum dislocation dynamics: towards a physical theory of crystal plasticity. J Mech Phys Solids 2014;63:167–78.
[24] Sandfeld S, Monavari M, Zaiser M. From systems of discrete dislocations to a continuous field description: stresses and averaging aspects. Modelling Simul Mater Sci Eng 2013;21(8):085006.
[25] Schmitt S, Gumbsch P, Schulz K. Internal stresses in a homogenized representation of dislocation microstructures. J Mech Phys Solids 2015;84:528–44.
[26] Lee S-H, Schulz K. A data-based derivation of the internal stress in the discrete-continuum transition regime of dislocation based plasticity. Int J Plast 2023;170:103771.
[27] Franciosi P, Berveiller M, Zaoui A. Latent hardening in copper and aluminium single crystals. Acta Metall 1980;28(3):273–83.
[28] Taylor GI. The mechanism of plastic deformation of crystals. Part I.—Theoretical. Proc R Soc Lond Ser A Contain Pap Math Phys Character 1934;145(855):362–87.
[29] Ern A, Guermond J-L. Theory and practice of finite elements, vol. 159, Springer; 2004.
[30] Butcher JC. Numerical methods for ordinary differential equations. John Wiley & Sons; 2016.
[31] Cockburn B. Discontinuous Galerkin methods. ZAMM-J Appl Math Mech/Z Angew Math Mech: Appl Math Mech 2003;83(11):731–54.
[32] Hartmann R. Numerical analysis of higher order discontinuous Galerkin finite element methods. 2008.
[33] Cockburn B, Shu C-W. Runge–Kutta discontinuous Galerkin methods for convection-dominated problems. J Sci Comput 2001;16:173–261.
[34] Saad Y, Schultz MH. GMRES: A generalized minimal residual algorithm for solving nonsymmetric linear systems. SIAM J Sci Stat Comput 1986;7(3):856–69.
[35] Wagner L. A discontinuous Galerkin method for continuum dislocation dynamics in a fully-coupled elastoplasticity model (Ph.D. thesis, Dissertation), Karlsruhe: Karlsruher Institut für Technologie (KIT); 2019.
[36] Toro EF. Riemann solvers and numerical methods for fluid dynamics: a practical introduction. Springer Science & Business Media; 2013.
[37] Kubin L, Devincre B, Hoc T. Modeling dislocation storage rates and mean free paths in face-centered cubic crystals. Acta Mater 2008;56(20):6040–9.
[38] Ledbetter HM, Naimon ER. Elastic properties of metals and alloys. II. Copper. J Phys Chem Ref Data 1974;3(4):897–935.
[39] Date EHF, Andrews KW. Anisotropic and composition effects in the elastic properties of polycrystalline metals. J Phys D: Appl Phys 1969;2(10):1373.
[40] Davey WP. Precision measurements of the lattice constants of twelve common metals. Phys Rev 1925;25(6):753.
[41] Kubin LP, Canova G, Condat M, Devincre B, Pontikis V, Bréchet Y. Dislocation microstructures and plastic flow: a 3D simulation. Solid State Phenom 1992;23:455–72.
[42] Cackett AJ, Hardie CD, Lim JJ, Tarleton E. Spherical indentation of copper: Crystal plasticity vs experiment. Materialia 2019;7:100368.
[43] Wang Y, Raabe D, Klüber C, Roters F. Orientation dependence of nanoindentation pile-up patterns and of nanoindentation microtextures in copper single crystals. Acta Mater 2004;52(8):2229–38.
[44] Liu Y, Wang B, Yoshino M, Roy S, Lu H, Komanduri R. Combined numerical simulation and nanoindentation for determining mechanical properties of single crystal copper at mesoscale. J Mech Phys Solids 2005;53(12):2718–41.

[45] Liu Y, Varghese S, Ma J, Yoshino M, Lu H, Komanduri R. Orientation effects in nanoindentation of single crystal copper. Int J Plast 2008;24(11):1990–2015.
[46] Hu D, Grilli N, Yan W. Dislocation structures formation induced by thermal stress in additive manufacturing: Multiscale crystal plasticity modeling of dislocation transport. J Mech Phys Solids 2023;173:105235.
[47] Nye JF. Some geometrical relations in dislocated crystals. Acta Metall 1953;1(2):153–62.
[48] Gurtin ME. A gradient theory of single-crystal viscoplasticity that accounts for geometrically necessary dislocations. J Mech Phys Solids 2002;50(1):5–32.